Quantum dynamic response-based NV-diamond magnetometry: Robustness to decoherence and applications in motion detection of magnetic nanoparticles

Wenkui Ding,[1,*] Xingyu Zhang,[2] Jing Liu,[3] Aixi Chen,[1] and Xiaoguang Wang[1,†]
[1]*Department of Physics, Zhejiang Sci-Tech University, 310018 Zhejiang, China*
[2]*Department of Physics, Xiamen University, 361005 Fujian, China*
[3]*MOE Key Laboratory of Fundamental Physical Quantities Measurement, National Precise Gravity Measurement Facility, School of Physics, Huazhong University of Science and Technology, Wuhan 430074, China*

(Received 17 July 2023; revised 11 June 2024; accepted 18 June 2024; published 1 July 2024)

We propose a quantum sensing protocol that leverages the dynamical response of physical observables to quenches in quantum systems. Specifically, we use the nitrogen-vacancy (NV) color center in diamond to realize both scalar and vector magnetometry via quantum response. Furthermore, we suggest a method for detecting the instantaneous motion of magnetic nanoparticles. To achieve this, we derive the closed exact form of the Berry curvature corresponding to NV centers and design quenching protocols to extract the Berry curvature via dynamical response. By constructing and solving nonlinear equations, the magnetic field and instantaneous motion velocity of the magnetic nanoparticle can be deduced. We investigate the feasibility of our sensing scheme in the presence of decoherence and show through numerical simulations that it is robust to decoherence. Intriguingly, we have observed that a vanishing nuclear spin polarization in diamond benefits our dynamic sensing scheme, which stands in contrast with conventional Ramsey-based schemes. In comparison with Ramsey-based sensing schemes, our proposed scheme can sense an arbitrary time-dependent magnetic field if its time dependence is nearly adiabatic.

DOI: 10.1103/PhysRevB.110.045202

I. INTRODUCTION

Quantum metrology [1–6] and quantum sensing [7–9] have attracted significant attention in recent years. Quantum sensors, leveraging the unique properties of quantum systems, hold promise for detecting weak or nanoscale signals that surpass the capabilities of classical sensors. While most quantum sensors rely on interference schemes, there are situations in which implementing interferometry or Ramsey-based schemes becomes challenging [10,11]. One such scenario arises when the signal to be detected exhibits a short period of viability, making it impractical to accumulate the necessary phase for information encoding in the interference-based scheme [12]. As a result, there is a growing emphasis on exploring mechanisms to realize innovative quantum sensing schemes, driving rapid developments in the field of quantum science and technology [6,13–17].

In recent studies [18–22], the concept of dynamical response has been proposed as a means to detect geometric quantities in quantum many-body systems. Notably, the emergence of Berry curvature in the nonadiabatic response of physical observables to slow quenches, irrespective of the interaction nature of the system, has been identified [18]. Building upon these findings, in this paper, we showcase the potential of utilizing the mechanism of dynamic response for quantum sensing, offering a complementary approach to the conventional interference-based sensing schemes. Specifically, we present quantum response-based sensing schemes utilizing nitrogen-vacancy (NV) color centers in diamond [23,24]. The NV center in diamond is a highly attractive candidate for quantum sensing due to its efficient initialization and readout capabilities through optical excitations as well as its relatively long coherence time, even at ambient temperature [25,26]. Consequently, extensive theoretical and experimental investigations have been conducted to explore the quantum sensing potential of NV centers [27–32]. Notably, NV centers have demonstrated the ability to sense magnetic fields with nanoscale spatial resolution [31,33]. Owing to their high spatial resolution, NV sensors have found applications in condensed matter physics, particularly for investigating the magnetic properties of mesoscopic systems. Notably, NV centers have been instrumental in sensing dynamic magnetic fields generated by moving spins, spin waves, or magnetic oscillations at the nanoscale. For example, single-spin magnetometry utilizing NV centers has been employed to investigate magnons in magnetic insulators [34]. Additionally, relaxometry techniques employing single NV sensors have enabled nanoscale imaging of magnetic order in antiferromagnetic materials [35]. NV magnetometry has also been applied to sense domain walls and skyrmion bubbles in thin-film systems [36]. Moreover, NV magnetometry has demonstrated the capability to detect individual proton spins on the surface of diamond with angstrom resolution, utilizing electron spins on the diamond surface and proximal NV centers within the diamond [37]. Furthermore, single-spin NV magnetometry has been employed to probe

*Contact author: wenkuiding@zstu.edu.cn
†Contact author: xgwang@zstu.edu.cn

magnetic fields generated by spin-torque oscillators in magnetic insulators [38].

Other geometric quantities, like the geometric phase, in NV centers have also been investigated [39,40] and proposed in applications in quantum sensing, like gyroscopes [41,42] and magnetometers [43]. Furthermore, owing to the chemical inertness and excellent quantum property under ambient conditions of diamond, NV sensors hold promise for applications in bioimaging [44]. In this paper, we propose an approach using NV centers through quantum dynamic response to sense the motion of magnetic nanoparticles, which has the potential to find applications in the field of bioimaging.

Before introducing the dynamic response-based sensing scheme, we provide a brief overview of the quantum response theory [18,21]. By employing adiabatic perturbation theory [19], the general formula for quantum response can be derived as follows (see Appendix A for detailed information):

$$M_\mu = \text{const.} + \sum_\lambda v_\lambda \mathcal{F}^{(m)}_{\mu\lambda} + \mathcal{O}\big(v_\lambda^2\big). \tag{1}$$

Here, M_μ represents the observable being measured in the experiment, often referred to as the generalized force along the μ direction. It can be defined as $M_\mu \equiv -\langle\psi(t_f)|\partial_\mu H|\psi(t_f)\rangle$, with $\partial_\mu H \equiv \partial H/\partial\mu$. The quantum state evolves according to $|\psi(t_f)\rangle = \mathcal{T}\exp[-i\int_0^{t_f} H(t')dt']|\Psi_m(0)\rangle$, where $\mathcal{T}$ denotes the time-ordering operator, and the time dependence of the Hamiltonian is introduced by the time-dependent parameters $H(t) = H[\lambda(t), \mu(t), \dots] \equiv H(\lambda, \mu, \dots)$. The initial state is prepared as one of the instantaneous eigenstates of the Hamiltonian $H(t)|\Psi_m(t)\rangle = E_m(t)|\Psi_m(t)\rangle$. The quench process is achieved by varying the parameter $\lambda(t)$ over time, with $v_\lambda \equiv \partial\lambda/\partial t$ representing the instantaneous quench velocity along the λ direction at time t_f. Notably, the Berry curvature $\mathcal{F}^{(m)}_{\mu\lambda}$ corresponding to the instantaneous eigenstate $|\Psi_m(t_f)\rangle$ emerges as the coefficient in the nonadiabatic response when the quench velocity approaches zero.

We would like to make some comments regarding the sensor utility of the quantum response formula presented in Eq. (1). The validity of this equation does not rely on the specific details of the quench process if the quench is performed in a nearly adiabatic manner. Most notably, this formula indicates that, by implementing quenches along the λ direction and measuring the corresponding response along the μ direction, we can extract the value of the Berry curvature $\mathcal{F}^{(m)}_{\mu\lambda}$. Since the Berry curvature is a geometric quantity solely determined by the parameter-dependent instantaneous eigenstate of the quantum system, it remains independent of the specific details of the quench process. Moreover, if the physical quantity of interest is encoded within the Berry curvature, we can determine its value by measuring the Berry curvature using the quench-response mechanism. Conversely, if the Berry curvature is known *a priori*, we can determine the instantaneous quench velocity by measuring the response of the system.

This paper is organized as follows: In Sec. II, we derive the closed exact form of the Berry curvature associated with NV centers. In Sec. III, we present a concrete dynamic response-based scheme for NV magnetometry and assess its feasibility by considering the effects of decoherence. In Sec. IV, we propose a protocol for detecting the motion of a magnetic nanoparticle using quantum response. In Sec. V, we investigate the sensitivity of our quantum response-based sensing scheme. Finally, summaries and discussions are made in Sec. VI.

II. BERRY CURVATURE OF NV CENTERS

Our focus centers on utilizing the NV center in diamond to realize dynamic response-based quantum sensing. In this section, we employ Sylvester's formula to derive a formalism of the Berry curvature, solely in terms of the eigenvalues of the parameter-dependent Hamiltonian. Then utilizing this formalism, we derive a closed exact analytic expression for the Berry curvature associated with NV centers. Finally, we demonstrate the quantum response scheme by applying a linear quench field.

A. Formalism of Berry curvature using Sylvester's formula

In general, the Berry curvature can be expressed as the imaginary part of the geometric tensor $\mathcal{F}_{\mu\lambda} = -2\Im[\chi_{\mu\lambda}]$. The geometric tensor $\chi_{\mu\lambda}$ is defined as follows [45]:

$$\chi_{\mu\lambda} = \langle\partial_\mu\Psi|\partial_\lambda\Psi\rangle - \langle\partial_\mu\Psi|\Psi\rangle\langle\Psi|\partial_\lambda\Psi\rangle, \tag{2}$$

where $|\partial_\lambda\Psi\rangle \equiv \frac{\partial|\Psi\rangle}{\partial\lambda}$, and $|\Psi\rangle \equiv |\Psi(\lambda,\mu)\rangle$ represents a parameter-dependent quantum state. When the parameter-dependent quantum state corresponds to the instantaneous eigenstates of the parameter-dependent Hamiltonian, given by $H(\lambda,\mu)|\phi_m(\lambda,\mu)\rangle = E_m(\lambda,\mu)|\phi_m(\lambda,\mu)\rangle$, the Berry curvature can be determined using the following expression:

$$\mathcal{F}^{(m)}_{\mu\lambda} = i\sum_{n\neq m} \frac{\langle\phi_m|\partial_\mu H|\phi_n\rangle\langle\phi_n|\partial_\lambda H|\phi_m\rangle - \langle\phi_m|\partial_\lambda H|\phi_n\rangle\langle\phi_n|\partial_\mu H|\phi_m\rangle}{[E_n(\lambda,\mu) - E_m(\lambda,\mu)]^2}, \tag{3}$$

assuming the eigenstate $|\phi_m\rangle$ is nondegenerate. This formula immediately indicates that $\mathcal{F}_{\lambda\lambda} = 0$ and $\mathcal{F}^{(m)}_{\lambda\mu} = -\mathcal{F}^{(m)}_{\mu\lambda}$.

Sylvester's formula states that any function $f(\hat{A})$ of the $n\times n$ matrix $\hat{A}$ with distinct eigenvalues λ_i can be represented as [46]

$$f\big(\hat{A}\big) = \sum_{i=1}^{n} f(\lambda_i)\hat{A}_i, \tag{4}$$

where

$$\hat{A}_i = \prod_{j\neq i} \frac{1}{\lambda_i - \lambda_j}(\hat{A} - \lambda_j\mathbf{1}). \tag{5}$$

Proof: Let us first consider the situation where $\hat{A}$ is a Hermitian matrix. Equation (4) suggests a resemblance to the

spectral decomposition:

$$f(\hat{A}) = \sum_{i=1}^{n} f(\lambda_i)|\psi_i\rangle\langle\psi_i|, \tag{6}$$

where $|\psi_i\rangle$ are the eigenvectors corresponding to the eigenvalues λ_i, i.e., $\hat{A}|\psi_i\rangle = \lambda_i|\psi_i\rangle$. To prove that $\hat{A}_i$ is indeed the projector $|\psi_i\rangle\langle\psi_i|$, we apply the completeness relation $\mathbf{1} = \sum_i |\psi_i\rangle\langle\psi_i|$ on the right-hand side of Eq. (5). This yields

$$\prod_{j\neq i} \frac{1}{\lambda_i - \lambda_j}(\hat{A} - \lambda_j \mathbf{1}) \sum_k |\psi_k\rangle\langle\psi_k| = |\psi_i\rangle\langle\psi_i|. \tag{7}$$

When $\hat{A}$ is non-Hermitian, we need to demonstrate that $\hat{A}_i = |\psi_{i,R}\rangle\langle\psi_{i,L}|$. The proof follows a similar approach, with the completeness relation now taking the form $\mathbf{1} = \sum_i |\psi_{i,R}\rangle\langle\psi_{i,L}|$, where $|\psi_{i,R}\rangle$ and $|\psi_{i,L}\rangle$ are the right and left eigenvectors, respectively. Notably, employing Eqs. (4) and (5), we can calculate the dynamics governed by a non-Hermitian Hamiltonian without needing to resort to a biorthogonal basis.

Upon examining the Berry curvature $\mathcal{F}^{(m)}_{\mu\lambda}$ in Eq. (3), it becomes apparent that $|\phi_n\rangle\langle\phi_n| = H_n$, where

$$H_n = \prod_{j\neq n} \frac{1}{E_n - E_j}(H - E_j \mathbf{1}). \tag{8}$$

Furthermore, we have $\langle\phi_m|\hat{X}|\phi_m\rangle = \mathrm{Tr}(|\phi_m\rangle\langle\phi_m|\hat{X})$. Consequently, we can express

$$\begin{aligned}
&\langle\phi_m|\partial_\mu H|\phi_n\rangle\langle\phi_n|\partial_\lambda H|\phi_m\rangle \\
&= \langle\phi_m|(\partial_\mu H)H_n(\partial_\lambda H)|\phi_m\rangle \\
&= \mathrm{Tr}[|\phi_m\rangle\langle\phi_m|(\partial_\mu H)H_n(\partial_\lambda H)] \\
&= \mathrm{Tr}[H_m(\partial_\mu H)H_n(\partial_\lambda H)].
\end{aligned} \tag{9}$$

As a result, the Berry curvature can be represented as

$$\begin{aligned}
\mathcal{F}^{(m)}_{\mu\lambda} &= i\sum_{n\neq m} \frac{\mathrm{Tr}\{\hat{X}^{(mn)}_{\mu\lambda} - [\hat{X}^{(mn)}_{\mu\lambda}]^\dagger\}}{(E_n - E_m)^2} \\
&= i\sum_{n\neq m} \frac{2\,\mathrm{Im}\{\mathrm{Tr}[\hat{X}^{(mn)}_{\mu\lambda}]\}}{(E_n - E_m)^2},
\end{aligned} \tag{10}$$

where $\hat{X}^{(mn)}_{\mu\lambda} \equiv H_m(\partial_\mu H)H_n(\partial_\lambda H)$, and it is assumed that $\partial_{\mu,\lambda}H$ are still Hermitian operators, which is generally appropriate. This result implies that, to calculate the Berry curvature using our formalism in Eq. (10) instead of Eq. (3), we only need to determine the corresponding eigenvalues of the parameter-dependent Hamiltonian, without resorting to the exact expression of the eigenvectors.

B. Berry curvature for NV centers

The Hamiltonian that describes the NV center driven by a time-varying magnetic field is given by [47]

$$\begin{aligned}
H(t) =& DS_z^2 + E(S_x^2 - S_y^2) \\
&+ g_e\mu_B \mathbf{h}(t)\cdot\mathbf{S} + \mathbf{S}\cdot\sum_{k=1}^{N}\mathbf{A}_k\cdot\mathbf{I}_k.
\end{aligned} \tag{11}$$

Here, $\mathbf{S} = (S_x, S_y, S_z)$ represents the spin operator of the NV electronic spin, which has a spin quantum number $S = 1$. The Hamiltonian contains several important terms: The first term represents the diagonal term of the zero-field splitting, and $D/\hbar \approx 2.87$ GHz represents the zero-field splitting parameter, which exhibits temperature dependence and can be exploited for temperature sensing. The second term corresponds to the off-diagonal term of the zero-field splitting, which captures the interaction between the electronic spin of the NV center and an external electric field or stress, providing a means for electric field and stress detection [48]. The third term corresponds to the Zeeman energy of the NV electronic spin in the presence of a time-varying magnetic field $\mathbf{h}(t) = [h_x(t), h_y(t), h_z(t)]$, while g_e is the NV electronic g factor and μ_B is the Bohr magneton. This term enables the sensing of magnetic fields. The last term describes the hyperfine interaction between the NV electronic spin and the surrounding nuclear spins, such as ^{13}C nuclear spins with a spin quantum number $I = \frac{1}{2}$. This term enables spin sensing, where $\mathbf{I}_k$ represents the spin operator of the kth nucleus and $\mathbf{A}_k$ represents the coupling strength of the NV electronic spin and the kth nuclear spin. The NV center in diamond possesses remarkable quantum properties, making it a versatile and promising quantum sensor under ambient temperature. While the last term is typically considered the origin of decoherence of the NV electronic spin, for the purpose of demonstrating our dynamic response-based sensing protocol, we temporarily neglect this coupling term. Its effect will be carefully investigated in the subsequent section.

By neglecting the last coupling term in Eq. (11), the simplified Hamiltonian can be expressed (by assuming $g_e\mu_B = 1$ for simplicity) as follows:

$$H = \begin{pmatrix} D + h_z & \frac{h_x - ih_y}{\sqrt{2}} & E \\ \frac{h_x + ih_y}{\sqrt{2}} & 0 & \frac{h_x - ih_y}{\sqrt{2}} \\ E & \frac{h_x + ih_y}{\sqrt{2}} & D - h_z \end{pmatrix}. \tag{12}$$

To obtain the analytic form of the Berry curvature using Eq. (3), we need to find the explicit eigenenergies of this parameter-dependent Hamiltonian. Fortunately, for a general 3×3 Hermitian matrix [49,50], since all the eigenvalues are real, we can analytically calculate them in terms of the trigonometric solutions (see Appendix B for more details). To be specific, the eigenvalues of the Hamiltonian in Eq. (12) can be obtained as follows:

$$\begin{aligned}
E_1 &= \frac{2}{3}\left[D - \Delta_0\cos\left(\frac{\varphi - \pi}{3}\right)\right], \\
E_2 &= \frac{2}{3}\left[D - \Delta_0\cos\left(\frac{\varphi + \pi}{3}\right)\right], \\
E_3 &= \frac{2}{3}\left[D + \Delta_0\cos\left(\frac{\varphi}{3}\right)\right],
\end{aligned} \tag{13}$$

where $\Delta_0 \equiv \sqrt{\frac{3}{2}\mathrm{Tr}[\mathcal{H}^2]}$ and $\cos\varphi = \frac{1}{2}(\frac{3}{\Delta_0})^3\det(\mathcal{H})$. Here, we have used the traceless Hamiltonian $\mathcal{H} \equiv H - \frac{\mathrm{Tr}[H]}{3}\mathbf{1}$,

with

$$\mathrm{Tr}[\mathcal{H}^2] = \frac{2}{3}D^2 + 2E^2 + 2h^2,$$
$$\det(\mathcal{H}) = \frac{2D}{3}\left(E^2 + h^2 - \frac{D^2}{9}\right) + h_x^2(E-D) - h_y^2(E+D),$$

where $h^2 = h_x^2 + h_y^2 + h_z^2$. An obvious advantage of this trigonometric analytic form is that it immediately reveals $E_1 \leqslant E_2 \leqslant E_3$ since $0 \leqslant \varphi \leqslant \pi$. To the best of our knowledge, the exact form of the eigenenergy of the NV Hamiltonian presented in this paper has not been utilized in the existing literature. Conventionally, discussions on the eigenenergies or transitions of the NV center, a three-level system, often rely on perturbation methods to obtain approximate results [8,23]. However, these approximate approaches can pose challenges when it comes to calculating the Berry curvature, which requires a more precise understanding of the eigenenergy structure of the system.

Equipped with the exact eigenenergies, we can now calculate the Berry curvature corresponding to the ground eigenstate using Eq. (10). After performing the involved yet straightforward calculations, we derive the analytical expression for the Berry curvature associated with NV centers when the Cartesian components of the magnetic field $h_{x,y,z}$ are employed as the driven parameters. The explicit forms of the Berry curvature components are given as follows:

$$\mathcal{F}_{xy}^{(1)} = \frac{9\sqrt{3}}{4\Delta_0^5}\frac{h_z}{\sin\varphi}\left[\frac{E_2(2D-E_2)}{\sin^2\frac{\varphi+\pi}{3}} - \frac{E_3(2D-E_3)}{\sin^2\frac{\varphi}{3}}\right], \tag{14}$$

$$\mathcal{F}_{xz}^{(1)} = \frac{9\sqrt{3}}{4\Delta_0^5}\frac{h_y}{\sin\varphi}\left[\frac{(D+E-E_3)(2E+E_3)}{\sin^2\frac{\varphi}{3}} - \frac{(D+E-E_2)(2E+E_2)}{\sin^2\frac{\varphi+\pi}{3}}\right], \tag{15}$$

$$\mathcal{F}_{yz}^{(1)} = \frac{9\sqrt{3}}{4\Delta_0^5}\frac{h_x}{\sin\varphi}\left[\frac{(D-E-E_3)(2E-E_3)}{\sin^2\frac{\varphi}{3}} - \frac{(D-E-E_2)(2E-E_2)}{\sin^2\frac{\varphi+\pi}{3}}\right]. \tag{16}$$

It is worth noting that these analytical results reveal some intriguing features. Specifically, when $h_z = 0$, we have $\mathcal{F}_{xy} = 0$, and similarly, when $h_x = 0$ ($h_y = 0$), we find $\mathcal{F}_{yz} = 0$ ($\mathcal{F}_{xz} = 0$).

With the explicit formulation of the Berry curvature at our disposal, we are now equipped to develop sensing protocols that harness the quantum dynamical response mechanism described by Eq. (1). In the subsequent sections, we will illustrate specific sensing schemes based on quantum response and thoroughly examine their feasibility. Through these investigations, we aim to establish the practicality and effectiveness of employing the quantum dynamical response for sensing applications.

C. Demonstration of a linear quench scheme

We proceed to examine a linear quench scheme where the magnetic field changes linearly along the x and z axes. Specifically, the linear quench field is given by $h_x(t) = h_{x0} + v_x t$, $h_y(t) = h_{y0}$, and $h_z(t) = h_{z0} + v_z t$. The initial state is prepared as the ground state of the initial Hamiltonian, and the response along the y axis is measured after evolving for a duration t_f. According to the quantum response formula in Eq. (1), we need to verify the following relation:

$$\langle\psi(t_f)|S_y|\psi(t_f)\rangle = \langle\Psi_1(0)|S_y|\Psi_1(0)\rangle + v_x\mathcal{F}_{xy}^{(1)} + v_z\mathcal{F}_{zy}^{(1)} + \mathcal{O}(v_x^2) + \mathcal{O}(v_z^2). \tag{17}$$

The left-hand side of Eq. (17) corresponds to the quantum response signal (depicted as the solid line in Fig. 1), where $|\psi(t_f)\rangle = \mathcal{T}\exp[i\int_0^t H(\tau)d\tau]|\Psi_1(0)\rangle$, with $\mathcal{T}$ denoting the time-ordering operator and $|\Psi_1(0)\rangle$ representing the ground state at the initial time. Meanwhile, the dashed line in Fig. 1 corresponds to the analytic result $\langle\Psi_1(0)|S_y|\Psi_1(0)\rangle + v_x\mathcal{F}_{xy}^{(1)} + v_z\mathcal{F}_{zy}^{(1)}$, namely, the right-hand side of Eq. (17) by neglecting the high-order terms. The Berry curvature $\mathcal{F}_{xy}^{(1)}$ and $\mathcal{F}_{zy}^{(1)}$ can be computed by substituting $h_x = h_x(t_f)$, $h_y = h_y(t_f)$, and $h_z = h_z(t_f)$ into Eqs. (14) and (16), respectively. The outcome displayed in Fig. 1 corroborates the quantum response theory. Evidently, as the quench velocity diminishes,

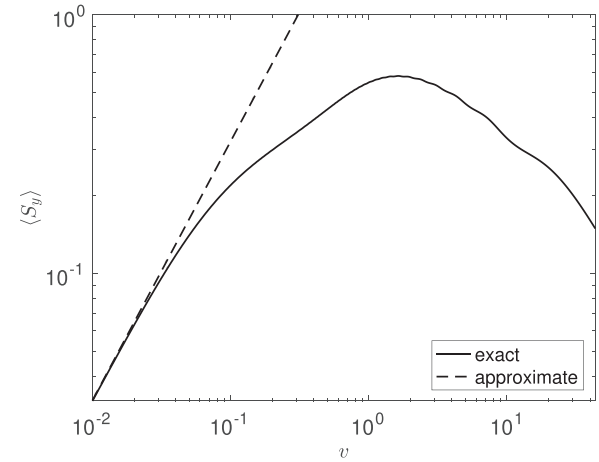

FIG. 1. Quantum response signal for a linear quench protocol. The parameters are set to $D = 0.9$, $E = 0.3$. The quench field is $h_x(t) = -10.5 + vt$, $h_y(t) = 0$, and $h_z(t) = -9.0 + vt$. Here, for simplicity, we have assumed $v_x = v_z = v$. The quantum response signal $\langle S_y\rangle \equiv \langle\psi(t_f)|S_y|\psi(t_f)\rangle$, with the measurement time $t_f = 10.0/v$.

the quantum response signal can be accurately approximated by the Berry curvature multiplied by the quench velocity.

III. SCALAR MAGNETOMETRY AND THE ROBUSTNESS TO DECOHERENCE

A. Berry curvature of the NV center in the spherical coordinate system

In this section, we present a specific scheme for scalar magnetometry utilizing the quantum response, focusing on a *rotating* quench protocol. Furthermore, we consider the simplified scenario where $E = 0$, which allows for a clear and concise presentation of the sensing procedure. Under these conditions, the Hamiltonian governing the dynamics of the NV center, driven by a magnetic field $\mathbf{h}(t) = h(\sin\theta\cos\phi, \sin\theta\sin\phi, \cos\theta)$, takes the form:

$$H = DS_z^2 + \exp(-i\phi S_z)\exp(-i\theta S_y)S_z \times \exp(i\theta S_y)\exp(i\phi S_z), \tag{18}$$

where we have adopted the convention of rescaling the zero-field coupling strength by setting $h = 1$, effectively incorporating it into the parameter $D/h \to D$. Utilizing the eigenenergy expression derived in Eq. (13), we can explicitly calculate the eigenenergies as follows:

$$E_1 = \frac{2}{3}\left[D - \sqrt{D^2+3}\cos\left(\frac{\varphi-\pi}{3}\right)\right],$$
$$E_2 = \frac{2}{3}\left[D - \sqrt{D^2+3}\cos\left(\frac{\varphi+\pi}{3}\right)\right],$$
$$E_3 = \frac{2}{3}\left[D + \sqrt{D^2+3}\cos\left(\frac{\varphi}{3}\right)\right], \tag{19}$$

where

$$\cos\varphi = \frac{D(-9-2D^2+27\cos^2\theta)}{2\sqrt{(D^2+3)^3}}. \tag{20}$$

Notably, the eigenenergies do not depend on the value of ϕ. Now we can employ Eq. (10) to explicitly calculate the Berry curvature $\mathcal{F}^{(1)}_{\phi\theta}$, with

$$\partial_\phi H = -\sin\theta\sin\phi S_x + \sin\theta\cos\phi S_y,$$
$$\partial_\theta H = \cos\theta\cos\phi S_x + \cos\theta\sin\phi S_y - \sin\theta S_z, \tag{21}$$

and

$$\mathrm{Tr}\{\hat{X}^{(12)}_{\phi\theta} - [\hat{X}^{(12)}_{\phi\theta}]^\dagger\} = \frac{iE_3\sin\theta[D\cos(2\theta)+3D-2E_3]}{(E_1-E_2)(E_1-E_3)(E_2-E_3)},$$
$$\mathrm{Tr}\{\hat{X}^{(13)}_{\phi\theta} - [\hat{X}^{(13)}_{\phi\theta}]^\dagger\} = -\frac{iE_2\sin\theta[D\cos(2\theta)+3D-2E_2]}{(E_1-E_2)(E_1-E_3)(E_2-E_3)}. \tag{22}$$

After some simplifications, the Berry curvature corresponding to the ground state becomes

$$\mathcal{F}^{(1)}_{\phi\theta} = \frac{9\sqrt{3}\sin\theta}{8(D^2+3)^{5/2}\sin\varphi}\left[\frac{E_3(D\cos 2\theta+3D-2E_3)}{\sin^2\left(\frac{\varphi}{3}\right)} - \frac{E_2(D\cos 2\theta+3D-2E_2)}{\sin^2\left(\frac{\varphi+\pi}{3}\right)}\right]. \tag{23}$$

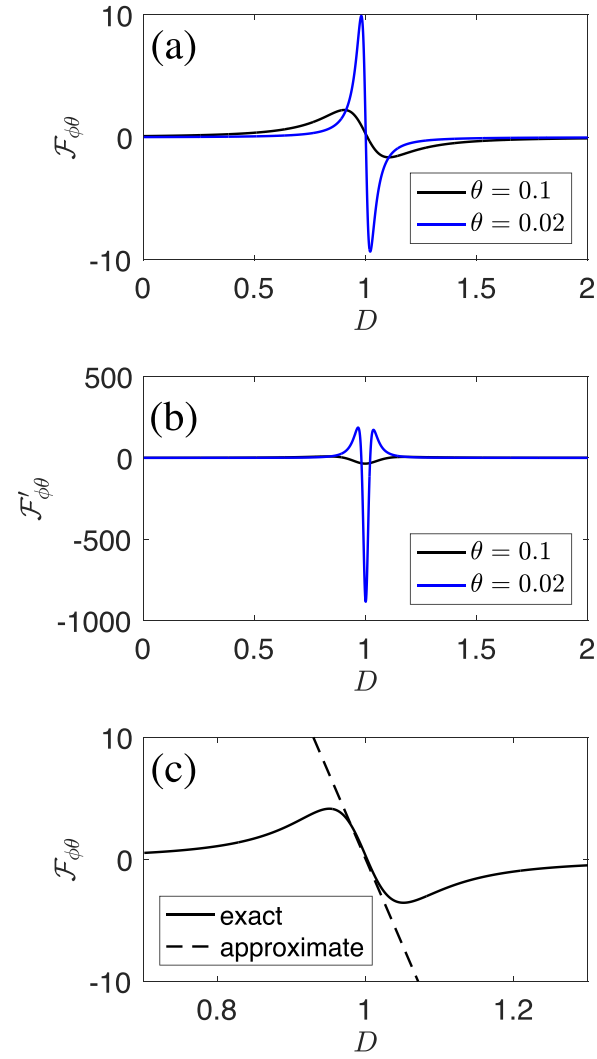

FIG. 2. Berry curvature and its susceptibility as functions of various NV parameters. (a) Berry curvature $\mathcal{F}_{\phi\theta}$ as a function of D with different values of θ. (b) Susceptibility of the Berry curvature $\partial\mathcal{F}_{\phi\theta}/\partial D$ as a function of D with different values of θ. (c) The Berry curvature can be approximated by a simple analytic form as $\theta \to 0$ when $D \sim 1$.

Based on this exact result, in Fig. 2, we plot the Berry curvature $\mathcal{F}_{\phi\theta} \equiv \mathcal{F}^{(1)}_{\phi\theta}$ and its susceptibility $\mathcal{F}'_{\phi\theta} \equiv \frac{\partial\mathcal{F}^{(1)}_{\phi\theta}}{\partial D}$ as functions of D with different values of θ. As shown in Fig. 2(a), the maximum value of the Berry curvature diverges as θ approaches zero. Accordingly, the susceptibility also diverges at $D = 1$, as shown in Fig. 2(b). This indicates the enhancement in the signal contrast at $D \sim 1$ when $\theta \to 0$. In fact, when $\theta \to 0$, we can derive an approximate analytic expression as follows (see Appendix C for a detailed derivation):

$$\mathcal{F}^{(1)}_{\phi\theta} \approx \frac{D-1}{2\sqrt{2}}\left(\frac{1}{\theta^2} - \frac{5}{32}\right). \tag{24}$$

This approximate analytic result immediately reveals the divergent feature in the Berry curvature and its susceptibility. As shown in Fig. 2(c), the exact result can be well approximated by this simple analytic expression when $D \sim 1$ and $\theta \to 0$.

B. Dynamic response-based sensing scheme using a rotating quench field

We now present a concrete quenching protocol to demonstrate how the quantum response-based sensing scheme operates. Different from the linear quench scheme in Sec. II C, here, we apply a rotating quench field given by

$$h_x(t) = \sin\left(\frac{v^2t^2}{2\pi}\right),$$
$$h_y(t) = 0,$$
$$h_z(t) = \cos\left(\frac{v^2t^2}{2\pi}\right). \tag{25}$$

Essentially, this is a quench along the θ direction, with $\theta(t) = \frac{v^2t^2}{2\pi}$. This choice of the rotating quench ensures that the driving at the initial time is adiabatic since $v_\theta(t=0)=0$. Specifically, we measure the response along the ϕ direction, namely, $\langle\partial_\phi H\rangle$, at $t_f = \pi/v$ with an instantaneous quench velocity of $v_\theta(t_f) = v$. Firstly, we perform numerical simulations to verify the validity of the quantum response formula stated in Eq. (1). For a rotating quench scheme, it asserts that

$$\langle\psi(t_f)|\partial_\phi H|\psi(t_f)\rangle = \langle\Psi_1(0)|\partial_\phi H|\Psi_1(0)\rangle + v_\theta\mathcal{F}^{(1)}_{\phi\theta} + \mathcal{O}[v_\theta^2], \tag{26}$$

where $|\psi(t_f)\rangle = \mathcal{T}\exp[-i\int_0^{t_f} H(t')dt']|\Psi_1(0)\rangle$. Here, the time-dependent Hamiltonian corresponds to the specific quench field in Eq. (25), and the quench duration is $t_f = \pi/v$. Since at the initial time the quantum system is prepared in the ground state, which is along the z axis, it immediately implies that $\langle\Psi_1(0)|\partial_\phi H|\Psi_1(0)\rangle = 0$. By applying Eq. (21), we find $\partial_\phi H = S_y$ at $t = t_f$. Additionally, when $\theta = \theta(t_f) = \pi/2$, the Berry curvature in Eq. (23) assumes a more compact form:

$$\mathcal{F}^{(1)}_{\phi\theta}\left(\phi, \theta = \frac{\pi}{2}\right) = D - \frac{D^2+2}{\sqrt{D^2+4}}. \tag{27}$$

Consequently, for the specific rotating quench protocol given by Eq. (25), to prove the quantum response formula in Eq. (26), we are aiming to verify that

$$\langle\psi(t_f)|S_y|\psi(t_f)\rangle = v\left(\frac{D^2+2}{\sqrt{D^2+4}} - D\right) + \mathcal{O}[v^2]. \tag{28}$$

In Fig. 3, the quantum response signal $\langle S_y\rangle \equiv \langle\psi(t_f)|S_y|\psi(t_f)\rangle$ is plotted as a function of the quench velocity $v_\theta(t_f) = v$ for various values of the zero-field splitting strength D. As depicted in the plot, the solid lines represent the exact numerical calculation of the dynamics governed by the time-dependent Hamiltonian for a given zero-field splitting D, while the dashed lines correspond to the analytic result obtained by multiplying the Berry curvature by the quench velocity. It is evident from the plot that, as the quench velocity approaches zero, the quantum response signal closely aligns with the analytic expression, which is the Berry curvature multiplied by the quench velocity.

Furthermore, upon comparing the quantum response signals for various zero-field splitting strengths, it is evident that, with a fixed variation in D, a larger quench velocity leads to a more significant change in the quantum response signal (note the logarithmic scale on the y axis). This suggests that increasing the quench velocity enhances the signal contrast, thereby benefiting the sensing scheme. However, as depicted in the figures, when the quench velocity increases even further, the quantum response signal will deviate from the analytic result. Consequently, in the quantum response-based sensing scheme, there exists an optimal quench velocity for estimating the parameter D to achieve the largest signal contrast.

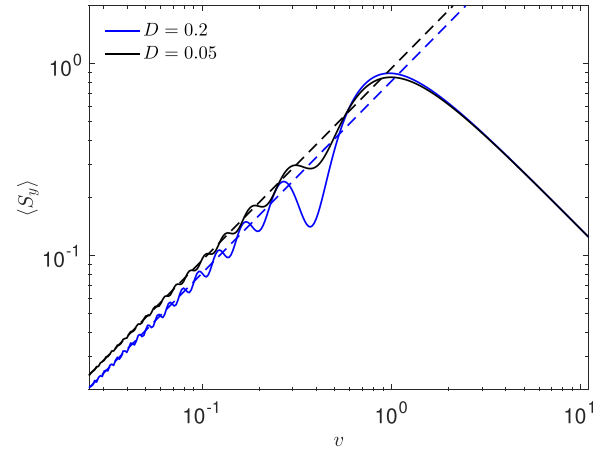

FIG. 3. Quantum response signal as a function of the quench velocity v for different values of the zero-field splitting D. To clarify, v denotes the instantaneous quench velocity along the θ direction at the measurement time t_f, denoted as $v_\theta(t_f) = v$. The solid lines correspond to the exact dynamics by numerically solving the time-dependent Schrödinger equation. The dashed lines correspond to the Berry curvature multiplied by the quench velocity on right-hand side of Eq. (28).

In Fig. 3, another noteworthy observation is the gradual emergence of oscillations as the quench velocity increases. This phenomena can be explained by employing the rotating reference frame (see Appendix D for a detailed discussion), where the spin vector adiabatically follows the linearly varying effective magnetic field when the quench velocity approaches zero. However, for a finite value of the quench velocity, the spin vector precesses about the effective magnetic field simultaneously, and the relative angle between the spin vector and the effective magnetic field depends on the quench velocity. Specifically, this angle increases as the quench velocity increases, leading to an increase in the oscillation amplitude, as shown in the plot.

In conclusion, Fig. 3 demonstrates that, as the quench velocity approaches zero, the quantum response signal can be accurately approximated by the Berry curvature multiplied by the quench velocity. To implement a realistic quantum response-based sensing scheme, it is essential to note that the quantity $\langle\psi(t_f)|S_y|\psi(t_f)\rangle$ can be measured in NV center experiments. Typically, an additional $\pi/2$ pulse is applied to measure $\langle S_z\rangle$ instead, utilizing spin state-dependent photoluminescence (PL) measurement of NV centers. After experimentally measuring $\langle\psi(t_f)|S_y|\psi(t_f)\rangle$, we can deduce the value of D or, equivalently, the magnitude of the magnetic field h, by solving the nonlinear equation in Eq. (28). This implementation enables quantum response-based magnetometry.

C. Robustness to decoherence of the sensing protocol

In this section, we examine the retrieval of the Berry curvature using quantum response in the presence of decoherence. Building upon the numerical simulation presented in Sec. III B, we extend our analysis to incorporate the influence of the environment, specifically the interaction with N nuclear spins. This interaction is captured by the inclusion of the last term in Eq. (11), which accounts for the coupling between the NV electronic spin and the nuclear spins. The presence of coupling to the nuclear spins introduces decoherence effects on the NV electronic spin, particularly when the nuclear spins are partially polarized. In this context, we consider the quenching process described by Eq. (25), and our objective is to calculate the response signal $M_y = \mathrm{Tr}[\rho(t_f)S_y]$ at $t_f = \pi/v$, where $\rho(t_f)$ is the state of the compound system $\rho(t_f) = U(t_f)\rho(0)U^\dagger(t_f)$. The time evolution operator $U(t_f) = \mathcal{T}\exp[-i\int_0^{t_f} H(t')dt']$, with $H(t)$ given by the Hamiltonian in Eq. (11). The initial state $\rho(0) = |\phi_0\rangle\langle\phi_0| \otimes \rho_n$ consists of two components: $|\phi_0\rangle\langle\phi_0|$, which corresponds to the ground state of the NV Hamiltonian in the absence of coupling to the nuclear spin bath, and ρ_n, which represents the initial state of the nuclear spin bath. The nuclear spin bath is assumed to be in a thermal state and is characterized by the density matrix $\rho_n = (1/Z)\exp(-\beta\sum_{k=1}^{N} I_{kz})$. Here, $Z = [2\cosh(\beta/2)]^N$ represents the partition function, and $\beta = 2\tanh^{-1}(P)$ denotes the inverse temperature, determined by the average nuclear polarization P [51].

When dealing with a large number of nuclear spins (N), simulating the dynamics governed by a time-dependent Hamiltonian using the density matrix formalism becomes computationally challenging due to the exponential growth of the Hilbert space dimension ($\sim 2^{N+1} \times 2^{N+1}$). To simplify the simulation for larger N, we employ certain approximations. First, we assume a homogeneous coupling between the NV electronic spin and the nuclear spins, namely, $\mathbf{A}_k = A$, based on the quasistatic approximation [52,53]. This allows us to utilize the collective nuclear spin operator $\mathbf{I} = \sum_{k=1}^{N} \mathbf{I}_k$, and the total angular momentum $\mathbf{J} = \mathbf{S} + \mathbf{I}$ becomes a constant of motion, leading to the reduction of the dimension of the Hilbert space. Second, since the initial state of the nuclear spins is assumed to be in a thermal state, we can employ wave function dynamics instead of density matrix calculations. Namely,

$$\rho(t_f) = \sum_{I_0=k}^{N/2} \sum_{M_0=-I_0}^{I_0} \omega(I_0, M_0)|\psi(t_f)\rangle\langle\psi(t_f)|, \qquad (29)$$

where $k = \frac{1}{2}$ if N is odd, and $k = 0$ if N is even. The time evolution of the wave function is given by $|\psi(t_f)\rangle = U(t_f)(|\phi_0\rangle \otimes |I_0, M_0\rangle)$, and the statistical weight associated with the nuclear spin state $|I_0, M_0\rangle$ is given by

$$\omega(I_0, M_0) = C_N^{(N/2)-I_0}\left(\frac{1+P}{2}\right)^{(N/2)-M_0} \times \left(\frac{1-P}{2}\right)^{(N/2)+M_0} \frac{2I_0+1}{\frac{N}{2}+I_0+1}, \qquad (30)$$

where C_N^M represents the binomial coefficient. By employing these simplifications, we can tackle the simulation of the dynamics in a more computationally feasible manner while capturing the essential features of the behavior of the system.

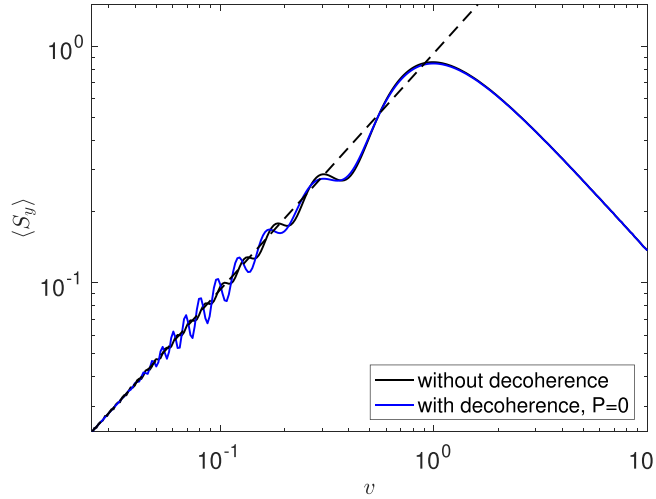

FIG. 4. Quantum response signal as a function of quench velocity with and without decoherence. The dashed line represents the analytic result expressed by the Berry curvature multiplied by the quench velocity. The black solid line corresponds to the quantum response signal without decoherence, obtained by exactly solving the dynamics governed by the Hamiltonian that neglects the coupling to nuclear spins. The blue solid line represents the quantum response signal in the presence of decoherence, obtained by solving the dynamics governed by the Hamiltonian in Eq. (11). In this simulation, we consider $N = 20$ nuclear spins, and the hyperfine coupling strength is set to $A_k = A = 0.02$. The nuclear spins are initially prepared in the maximal thermal state with a nuclear polarization of $P = 0$. Additionally, other common parameters are set to $E = 0$ and $D = 0.06765$.

After making the simplifications mentioned above, we perform simulations of the quantum response experiment considering $N = 20$ nuclear spins (with spin $I = \frac{1}{2}$). In Fig. 4, we compare the quantum response signal with and without decoherence. In accordance with Fig. 3, the black solid line represents the quantum response signal without decoherence, while the dashed line corresponds to the analytic result obtained by multiplying the Berry curvature with the quench velocity. Meanwhile, the blue solid line in Fig. 4 represents the quantum response signal when decoherence effects are considered, accounting for the coupling to nuclear spins. In this plot, the nuclear spins are assumed to be in the maximal thermal state, with a nuclear polarization of $P = 0$, which serves as a reasonable approximation under ambient temperature conditions. The close alignment of the blue solid line with the dashed line signifies that, even in the presence of docoherence, the quantum response signal can still be well approximated by the product of the Berry curvature and the quench velocity. In fact, this characteristic is in accordance with the adiabatic perturbation theory, which states that certain forms of decoherence, such as dephasing in quantum systems, do not significantly impact the validity of the quantum response formula (see Ref. [18]). Additionally, the coupling to nuclear spins induces fluctuations in the effective magnetic field experienced by NV spins, resulting in more pronounced oscillations than the case without considering decoherence. We

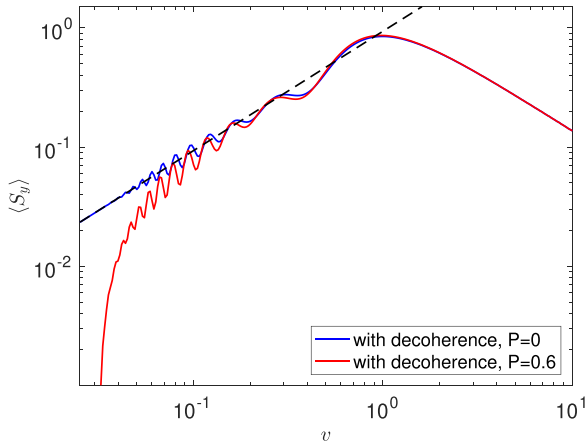

FIG. 5. Quantum response signals in the presence of decoherence with different nuclear polarizations. The dashed line and the black solid line correspond to the same lines in Fig. 4. Here, the red solid line represents the quantum response signal obtained by exactly solving the dynamics with a nuclear polarization $P = 0.6$. Other common parameters are kept consistent with those in Fig. 4.

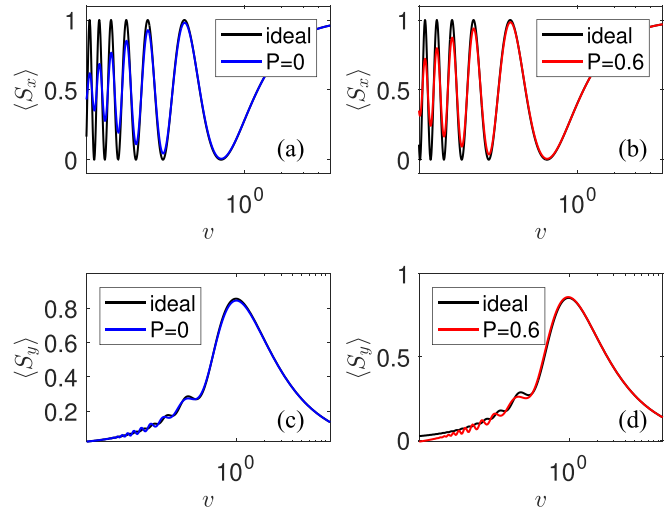

FIG. 6. Comparison of the effect of nuclear polarization on the quantum response-based sensing scheme and the Ramsey sensing scheme. (a) and (b) correspond to the Ramsey sensing scheme, where $\langle S_x \rangle \equiv \langle S_x(t) \rangle + \frac{1}{2}$ represents the normalized spin expectation value. Here, $\langle S_x(t) \rangle$ is given by Eq. (E8) in Appendix E. The effective quench velocity is defined as $v = 1/t$, where t is the interrogation time for the Ramsey scheme. The black solid line represents the ideal case, neglecting decoherence due to the flip-flop term in the hyperfine coupling. The blue and red solid lines represent the Ramsey sensing signal in the presence of decoherence with nuclear polarization $P = 0$ and 0.6, respectively. It is evident that the red line ($P = 0.6$) is much closer to the ideal case than the blue line ($P = 0$), indicating that high nuclear polarization is beneficial for the conventional Ramsey sensing scheme. The parameters for the calculations are fixed as follows: $h_0 = 2$, $N = 20$, and $A = 0.04$. (c) and (d) correspond to the signal of the quantum response-based sensing scheme. The black solid line represents the ideal case in the absence of decoherence. The blue and red lines correspond to cases in the presence of docoherence with nuclear polarization $P = 0$ and 0.6, respectively. These two lines are in accordance with the respective lines in Fig. 5. For the quantum response-based sensing scheme, it is clear that the blue line ($P = 0$) is much closer to the ideal case than the red line ($P = 0.6$), indicating that a vanishing nuclear polarization is beneficial for the quantum response-based sensing scheme instead.

will further elucidate these phenomena from the perspective of effective nuclear fields later.

Furthermore, in Fig. 5, we present a comparison of the quantum response signal in the presence of decoherence under varying degrees of nuclear polarization. Notably, when the nuclear polarization is finite, represented by the red solid line with $P = 0.6$, the exactly calculated quantum response signal deviates from the analytic result (depicted by the dashed line) as the quench velocity decreases. This observation suggests that increasing the nuclear polarization will degrade the effectiveness of the quantum response-based sensing scheme, which relies on the accuracy of the quantum response formula. In contrast, in a conventional Ramsey sensing scheme operating in the presence of decoherence, high nuclear polarization is typically required to attain heightened sensitivity. In Appendix E, we have a comprehensive discussion on the impact of nuclear polarization on the Ramsey sensing scheme. To better illustrate the different characteristics of these sensing schemes, we present Fig. 6, which shows the sensing signals as a function of (effective) quench velocities under varying levels of nuclear polarization. It is evident that, for the Ramsey scheme, the sensing signal approaches the ideal case (neglecting decoherence caused by the flip-flop terms in the hyperfine interaction) as nuclear polarization increases. On the other hand, for the quantum response-based sensing scheme, the sensing signal approaches the ideal case as the nuclear polarization becomes vanishingly small. Typically, achieving a high level of nuclear spin polarization in solid-state systems is challenging due to the small gyromagnetic ratio of nuclear spins and their weak coupling to the environment. Furthermore, the overhead associated with the buildup time for nuclear polarization presents another obstacle, as it can reduce the overall sensitivity of the quantum sensor. For example, in Ref. [54], a polarization of $P = 0.7$ was reported for the proximal ^{13}C nuclear spins in diamond, and it needs a typical time of tens of seconds to polarize bulk ^{13}C nuclear spins. In summary, while a vanishing nuclear polarization will reduce the sensitivity of the Ramsey sensor, it proves advantageous for the quantum response-based sensing scheme. This characteristic highlights the robustness of the quantum response-based sensing scheme to decoherence, indicating its potential advantages for implementation in realistic solid-state spin systems since no nuclear polarization is required.

Now we provide explanations for the observed behavior of the quantum response signals in the presence of decoherence, as depicted in Figs. 4 and 5, from the perspective of effective nuclear field. In our simulation, the decoherence of the electronic spin arises from the hyperfine coupling with the surrounding nuclear spins. According to Eq. (11), the hyperfine interaction is expressed as $H_{\rm hf} = \mathbf{S} \cdot \sum_{k=1}^{N} A\mathbf{I}_k$, with the assumption of homogeneous coupling strength ($A_k = A$). In fact, the hyperfine coupling can be decomposed into two distinct components: the dephasing part $H_{\rm dephase} = S_z \sum_{k=1}^{N} A I_k^z$ and the flip-flop part $H_{\rm flip\text{-}flop} = \frac{A}{2} \sum_{k=1}^{N} (S_+ I_k^- + S_- I_k^+)$. In

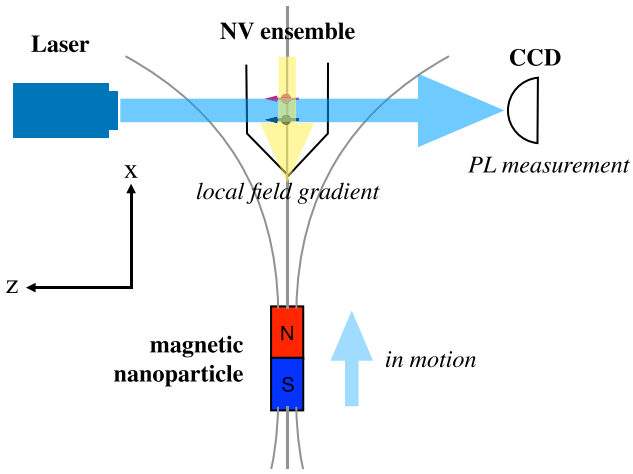

FIG. 7. Sensing the motion of the magnetic nanoparticle via quantum dynamic response. The NV ensemble in the diamond is optically initialized by illuminating it with a 532 nm laser, and the electronic spin state of the NV center can be determined by the spin-state-dependent photoluminescence (PL). The static local field gradient can be introduced by mounting a nanomagnet onto the diamond. Generally, the magnetic nanoparticle can be in the Brownian motion, but here, we restrict the motion of the magnetic nanoparticle along the x axis for clarity.

situations where the resonance condition is not satisfied [51], as in our simulations, the flip-flop term is typically suppressed, and the dephasing term assumes dominance. Alternatively, from a different perspective, the dephasing term can be interpreted as the coupling of the electronic spin with an effective nuclear field, given by $H_{\text{dephase}} = \hat{B}_N S_z$, where $\hat{B}_N = \sum_{k=1}^{N} A I_k^z$. When the initial state of the nuclear spins is in a thermal state with nuclear polarization P, it can be verified that the average value of the nuclear field is $\langle \hat{B}_N \rangle = NAP/2$, while the variance of the nuclear field is $\langle \Delta \hat{B}_N \rangle = NA^2(1-P^2)/4$. As depicted in Fig. 4, when the average nuclear field is zero for $P = 0$, the dephasing within the quantum system does not invalidate the quantum response formula, although the nonzero fluctuation of the nuclear field results in an increase in the amplitude of the oscillations. In contrast, as illustrated in Fig. 5, when $P = 0.6$, the average nuclear field becomes nonzero. This finite nuclear field, coupled with its fluctuations, leads to deviations of the quantum response signal from the analytic result.

IV. VECTOR MAGNETOMETRY AND MOTION SENSING OF MAGNETIC NANOPARTICLES

In recent years, several proposals have been put forward to realize vector magnetometry using solid-state spins [28,55–58]. In this section, we present a concrete example to demonstrate the implementation of vector magnetometry and the motion sensing of magnetic nanoparticles using NV centers in diamond through quantum dynamic response. The schematic diagram in Fig. 7 illustrates the setup, where NV centers are utilized to sense the motion of a magnetic nanoparticle and determine the instantaneous magnetic field generated by the magnetic nanoparticle itself [59]. Typically, the magnetic nanoparticle undergoes Brownian motion, leading to a time-varying magnetic field experienced by the NV center. By formulating equations based on the quantum response formula, we can, in principle, determine the motion of the magnetic nanoparticle for arbitrary time dependencies if the motion is nearly adiabatic. Here, for clarity, we restrict the motion of the magnetic nanoparticle along the x axis to demonstrate the capability of the vector magnetometry and the motion sensing. We now consider two ensembles of NV centers, and the Hamiltonian for the NV center in the ith ensemble is given by

$$H^{(i)}(t) = DS_z^2 + h_z^{(i)} S_z + h_y S_y + h_x(t) S_x. \tag{31}$$

Here, $h_z^{(i)}$ represents the static magnetic field applied to the ith ensemble along the z axis. Since these two ensembles of NV centers are usually close to each other, this different static field can be generated by mounting a nanomagnet on the diamond. The static magnetic field h_y is common to both NV ensembles. The static fields $h_z^{(i)}$ and h_y are assumed to be known beforehand, which can be determined, for example, through conventional Ramsey-based magnetometry. The magnetic field $h_x(t)$, which we aim to detect, is generated by the magnetic nanoparticle. Initially, at time $t = 0$, the magnetic nanoparticle is far away from the NV center, resulting in a negligible value for $h_x(t = 0)$. The initial state of the NV center is prepared in its ground state, which can be optically polarized by illuminating a 532 nm laser [26,60].

When the magnetic nanoparticle moves in close proximity to the NV center, the NV center experiences a time-varying magnetic field $h_x(t)$ along the x axis. At a specific measurement time t_f, we perform measurements on the spin-expectation values of the two NV ensembles, denoted as $\langle S_z^{(1)} \rangle$ and $\langle S_z^{(2)} \rangle$, utilizing spin-state-dependent PL [26]. According to the quantum response formula, the relationship between these measured spin-expectation values and the magnetic field components can be described by the following equations:

$$\begin{aligned} \langle S_z^{(1)} \rangle &= v_x \mathcal{F}_{xz}^{(1)}[h_x(t_f), h_y, h_z^{(1)}] + \mathcal{O}[v_x^2], \\ \langle S_z^{(2)} \rangle &= v_x \mathcal{F}_{xz}^{(1)}[h_x(t_f), h_y, h_z^{(2)}] + \mathcal{O}[v_x^2], \end{aligned} \tag{32}$$

where the Berry curvature $\mathcal{F}_{xz}^{(1)}[h_x, h_y, h_z^{(i)}]$ is determined by Eq. (15) and v_x is the quench velocity. By solving these nonlinear equations, we can obtain the instantaneous values of the magnetic field h_x and the velocity v_x at time t_f. From the perspective of motion sensing, the proposed method allows us to determine the instantaneous velocity of the magnetic nanoparticle and extract valuable information about its position by determining the magnetic field h_x. In other words, by constructing groups of these nonlinear equations using static field gradients, we eliminate the need to know the quench velocity beforehand to estimate the magnetic field. The vector magnetometry can be realized in the same manner. For instance, in the case where the value of h_y is not known in advance, we can extend the setup by incorporating an additional ensemble of NV centers with a different $h_z^{(i)}$. This allows us to construct an additional nonlinear equation, enabling the determination of h_y as well. Specifically, by applying an additional ensemble of NV centers, an extra equation, given by $\langle S_z^{(3)} \rangle = v_x F_{xz}^{(1)}[h_x(t_f), h_y, h_z^{(3)}] + \mathcal{O}[v_x^2]$, can be added to

Eq. (32). Now with these three equations at our disposal, the three unknowns (h_x, h_y, v_x) can be determined by numerically solving this set of equations. Once the components of the magnetic field (h_x, h_y) are determined, this indicates that vector magnetometry has been successfully implemented.

In the particle motion detection protocol depicted in Fig. 7, employing multiple NV centers serves a role analogous to applying reference fields in standard Ramsey vector magnetometry. In principle, the protocol requires only two settings of the NV ensembles to extract both the magnetic field strength and the quench velocity. Indeed, the extraction of the magnetic field components and the quench velocity involves solving equations derived from both the quantum response formula and the analytic form of the Berry curvature. As the number of unknown components of the magnetic field increases, it becomes necessary to utilize multiple NV ensembles. Furthermore, instead of applying reference fields successively, the utilization of multiple NV ensembles offers the benefit of enhancing the temporal resolution of the sensing scheme. If the NV ensembles are too far apart, the spatial resolution of the sensing scheme may be compromised. Conversely, if they are placed too close together, the diffraction limit of the microscope (or the CCD) becomes a limiting factor. Consequently, there exists an optimal range of distances for the spatial distribution of NV ensembles, typically spanning a few micrometers.

As depicted in Figs. 1 and 3, it is imperative to ensure the validity of the quantum response formula that the quench velocity of the magnetic field remains sufficiently small, approaching the adiabatic condition. In the realm of motion sensing of magnetic nanoparticles, this quench velocity is intricately linked to both the velocity of the nanoparticle and the magnetic field gradient, which is contingent upon the specific shape of the nanoparticle. Consequently, the upper bound of the range of nanoparticle velocities that can be effectively detected is predominantly determined by the imperative to maintain the validity of the quantum response formula as well as the field gradient generated by the magnetic particle. Meanwhile, the lower bound of the quench velocity is constrained by the longitudinal relaxation time T_1, as relaxation to the ground state can compromise the validity of the quantum response formula. For the NV spin in diamond, the typical longitudinal relaxation time T_1 ranges from several milliseconds to several seconds [8]. The detection speed of NV centers imposes an additional constraint on the detectable range of nanoparticle velocity. When the interrogation time of the optical signal is much shorter than the evolution time of the quantum response-based sensing scheme, the impact of this constraint can be negligible. The NV-diamond magnetometry proposal in Ref. [61] estimated the optical readout time $t_R \sim 2\,\mu$s. Additionally, Table V in Ref. [8] lists the readout times used for the optical readout of NV centers across various experimental setups. These timescales range from submicrosecond to several microseconds. To achieve high sensing accuracy, the parameters to be estimated, such as the motion velocity and the magnetic field, should remain relatively constant during the spin readout duration. For instance, in the sensing scheme presented in Fig. 7, the quench velocity is fixed during the spin readout duration, while the variation of the magnetic field depends on the motion velocity and the field gradient (which in turn is determined by the shape of the magnetic nanoparticle). Consequently, the combination of the shape of the nanoparticle and the spin readout duration determines the upper bound of the quench velocity that can be accurately detected. By considering both the upper and lower bounds together, we can effectively estimate the detectable range of nanoparticle velocity.

In conclusion, we present a sensing proposal for detecting the motion of magnetic nanoparticles based on the mechanism of quantum dynamic response. This approach enables us to realize highly sensitive motion sensing within nanoscale, where the position and instantaneous velocity of the magnetic nanoparticle can be determined through the analysis of the measured spin expectation values. It offers a promising avenue for accurately tracking and characterizing the motion of nanoscale objects using solid-state spins. This has significant implications in various fields, including bioimaging, where magnetic nanoparticles can serve as indicators for targeted imaging [44,59]. Additionally, the quantum response-based sensing protocol provides high temporal resolution, namely, it can measure the instantaneous value of the magnetic fields. Combined with the high spatial resolution of the NV sensors, our sensing scheme may be adapted to sense the dynamic fields within nanoscale. For instance, by placing the NV center close to a nanowire, our quantum response-based sensing scheme may be applied to sense the Oersted fields [62], the domain-wall motion [63], the Barkhausen effect [64], etc.

Now we conduct a comparative analysis between the quantum response-based sensing scheme and the conventional sensing scheme employing interference to detect motion by NV centers in diamond. In Ref. [65], by coupling the mechanical motion of a levitated micromagnet to the NV spin, the motion of the magnet is sensed by measuring the peak in the power spectral densities of the NV PL counts. Similarly, spin readout of the particle libration was demonstrated [66] by coupling the librational mode of the levitating ferromagnetic particles to the NV spin in diamond. The proposal in Ref. [67] puts forth a strategy leveraging a single NV spin magnetometer to detect the quantum motion of a mechanical oscillator through magnetic coupling, akin to spin-echo-based ac-magnetometry techniques. Essentially, these methodologies aim to perceive the motion of micromagnets by detecting the time-varying magnetic field they generate via either NV ac or dc magnetometry. However, it is important to note that these schemes do not correspond to standard continuous position measurement. Instead, they focus on discerning the fluctuations in the positions of the magnetic oscillators, without providing direct information about the instantaneous position of the micromagnet. In essence, while these methods excel at detecting the dynamic variations in the position of the micromagnet, they lack the high temporal resolution required to precisely determine its motion at any given instant.

V. INVESTIGATION ON THE SENSITIVITY

In this section, we investigate the sensitivity of our dynamic response-based sensing scheme, specifically focusing on the sensing scheme discussed in Sec. III. By analyzing the closed exact form of the Berry curvature given in Eq. (23), we can calculate the susceptibility of the Berry curvature with

respect to the parameter D. This susceptibility corresponds to the signal contrast. Remarkably, we can analytically calculate the susceptibility as θ approaches zero when $D = 1$. In this limit, the susceptibility exhibits the following behavior:

$$\lim_{\theta\to 0}\frac{\partial}{\partial D}\left[\frac{9\sqrt{3}\sin\theta E_3(D\cos 2\theta+3D-2E_3)}{8(D^2+3)^{5/2}\sin\varphi\sin^2\left(\frac{\varphi}{3}\right)}\right]=\infty,$$
$$\lim_{\theta\to 0}\frac{\partial}{\partial D}\left[\frac{9\sqrt{3}\sin\theta E_2(D\cos 2\theta+3D-2E_2)}{8(D^2+3)^{5/2}\sin\varphi\sin^2\left(\frac{\varphi+\pi}{3}\right)}\right]=-\frac{1}{8\sqrt{2}}, \tag{33}$$

which indicates that

$$\lim_{\theta\to 0}\frac{\partial\mathcal{F}^{(1)}_{\phi\theta}}{\partial D}=\infty. \tag{34}$$

This reveals that, near the work point ($\theta = 0, D = 1$), a slight change in D will result in a significant variation in the Berry curvature $\mathcal{F}^{(1)}_{\phi\theta}$, which corresponds to a measurable quantity divided by the quench velocity in the experiment. Consequently, we anticipate an exceptionally high sensitivity near the work point in our dynamic response sensing scheme. This is reminiscent of the sensor utility of non-Hermitian systems, where the susceptibility of certain measurable quantities can also exhibit divergent behaviors [14,15].

However, it is important to note that the work point ($\theta = 0, D = 1$) corresponds to an energy-degenerate point ($E_1 = E_2$). Thus, achieving near adiabatic conditions when approaching this point requires an extremely small quenching velocity. Consequently, while the susceptibility near the work point may be divergent, it is accompanied by a significantly longer evolution time. Therefore, the divergence in susceptibility does not necessarily translate into a divergence in sensitivity. In fact, a general bound for the estimation uncertainty has been proposed in Ref. [68] for dynamic quantum sensing schemes, considering the evolution time explicitly. When the parameter encoding process (for both sudden quench and adiabatic quench) is governed by the parameter Hamiltonian $\hat{H}_\lambda$, this bound is given by

$$\delta\lambda \geqslant \frac{1}{t\left|\left|\frac{\partial\hat{H}_\lambda}{\partial\lambda}\right|\right|}, \tag{35}$$

where $||\hat{A}||$ represents the seminorm defined as the difference between the maximum and minimum eigenvalues of the operator $\hat{A}$, i.e., $||\hat{A}|| = E_{\max} - E_{\min}$. In the dynamic sensing protocol described in Sec. III, the ultimate sensitivity bound for estimating the parameter D is given by $\delta D \geqslant 1/t$.

Since both our dynamic response-based sensing scheme and the conventional Ramsey-based sensing scheme are subject to the same ultimate sensitivity bound as described by Eq. (35), the divergence in the susceptibility of the Berry curvature presented in Eq. (34) does not necessarily imply a divergent sensitivity. Hence, our dynamic response-based sensing scheme does not offer an inherently enhanced ultimate sensitivity compared with the Ramsey-based scheme. However, the advantage of our dynamic response-based sensing scheme lies in its capability to sense time-varying magnetic fields or the motion of magnetic nanoparticles with very high temporal resolution. As discussed in the previous section, conventional interference-based sensing schemes face challenges in detecting instantaneous motions effectively. Consequently, the quantum response-based sensing scheme presents opportunities for applications in dynamic sensing scenarios, where conventional schemes may prove insufficient.

VI. DISCUSSION AND SUMMARY

The essence of our dynamic response-based sensing scheme lies in utilizing the dynamics governed by a *time-dependent* Hamiltonian to encode the parameter of interest into the quantum state. Usually, calculating the dynamics governed by a time-dependent Hamiltonian, like using the time-ordering evolution operator, can be challenging, limiting its application in quantum sensing. However, the quantum response theory offers a valuable tool by providing a simple and clear expression of the observable dynamics in terms of the Berry curvature if the time dependence of the Hamiltonian is near adiabatic. In this paper, we leverage this relation to demonstrate the power of the quench-response mechanism in realizing quantum sensing. Unlike conventional interference or Ramsey-based sensing schemes, which rely on time-independent Hamiltonians to encode the parameter, our dynamic response-based sensing scheme offers distinct advantages. It enables the sensing of instantaneous magnetic fields and the detection of the real-time motion of magnetic nanoparticles. This capability opens up possibilities in quantum sensing, particularly in scenarios where the parameter to be estimated are time dependent and require real-time measurements.

In this paper, we employ the NV center in diamond as our platform to demonstrate the effectiveness of the dynamic response-based sensing scheme. By analytically deriving the exact form of the Berry curvature, we can design quench-response protocols that enable us to accurately estimate the magnitude of the magnetic field or the quench velocity. One of the notable advantages of our dynamic response-based sensing scheme is its robustness to decoherence. Contrary to conventional interference-based approaches, we find that a vanishing nuclear polarization actually benefits our scheme. This counterintuitive result highlights the unique properties of the dynamic response-based approach and its resilience to decoherence effects. This robustness is a significant advantage, making our scheme highly feasible for realistic experiments, as nuclear polarization invariably demands additional resources. Furthermore, by exploiting the quench-response mechanism, we propose schemes that enable the detection and characterization of the motion of magnetic nanoparticles. This advancement opens up possibilities for applications in bioimaging and other areas where accurate motion tracking within nanoscale is essential.

By measuring the geometric phase, dc magnetometry has been implemented using NV centers [43]. While both this geometric phase magnetometry technique and our quantum response-based sensing scheme rely on measuring geometric quantities such as Berry phase or Berry curvature, they exhibit distinct characteristics. Our findings indicate that the quantum response-based sensing scheme offers superior temporal resolution and robustness to decoherence, while geometric

phase magnetometry enables wide-dynamic-range magnetic field sensing by eliminating the phase ambiguity. In Ref. [12], NV centers within diffusing nanodiamonds were utilized to detect the rotation of the entire sensor package. While this protocol primarily estimates physical quantities through the determination of geometric phase, it is worth noting that the quantum response mechanism may offer an alternative avenue for sensing applications. In Ref. [69], the intrinsic and induced quantum quenches is incorporated to the standard T_2-type qubit-based quantum noise spectroscopy (QNS). In this approach, a quench-induced phase shift is applied to investigate the properties of the environment. The primary distinction between the quench-enhanced QNS and our quantum response-based sensing scheme lies in the target of the quenches. In the former, quenches are applied to the environment, whereas in the latter, quenches are applied solely to the system. Furthermore, the quench-enhanced QNS aims to estimate properties such as temperature of the environment, which are encoded in the initial state. By comparison, our quantum response-based sensing scheme estimates parameters incorporated in the Hamiltonian, like external fields. Essentially, the time evolution of the quench-enhanced QNS scheme is governed by a time-independent Hamiltonian after the sudden change at the initial time. In contrast, the time-evolution of our quantum response-based sensing scheme is governed by a time-dependent Hamiltonian. This difference signifies that the quench-enhanced QNS employs a sudden quench, while our quantum response-based scheme employs an adiabatic quench. Moreover, in Ref. [20], the response of a driven open system governed by adiabatically evolving Lindbladians is investigated. In this paper, the response associated with observables is connected with the Fubini-Study metric and the Berry curvature. The theory presented in this paper may also be applied to estimate properties of the environment, such as the dephasing rate.

In fact, the principle of our dynamic sensing scheme can be extended to other quantum systems, including quantum many-body systems, whether they are interacting or not. While the exact form of the Berry curvature may not be obtainable in these systems, it can still be measured experimentally through alternative methods [70,71] or via the quantum response theory introduced here. By measuring the value of the Berry curvature in advance, we can design dynamic sensing protocols to detect the quench velocity in these systems. The dynamic response-based sensing scheme proposed in this paper offers the advantage of technical simplicity, making it highly accessible for practical implementation in experimental settings. In this paper, we demonstrate the potential of utilizing the dynamic response and the quench-response mechanism to realize a sensing scheme. However, there are still untapped possibilities and further potentials to explore in the field of quantum sensing using this approach. Future researchers can delve deeper into these unexplored avenues and uncover applications and insights.

ACKNOWLEDGMENTS

This paper was supported by the National Key Research and Development Program of China (Grants No. 2017YFA0304202 and No. 2017YFA0205700); the NSFC through Grants No. 11875231, No. 11935012 and No. 12305031; and the Fundamental Research Funds for the Central Universities through Grant No. 2018FZA3005.

APPENDIX A: REVIEW OF THE QUANTUM RESPONSE THEORY

To render this paper more self-consistent, we now make a brief review on the adiabatic perturbation theory and the quantum response theory. More details can be found in Refs. [18,19,21]. The Schrödinger equation for a time-dependent Hamiltonian is

$$i\frac{\partial|\psi(t)\rangle}{\partial t} = H(t)|\psi(t)\rangle. \tag{A1}$$

Here, we expand the wave function using the instantaneous eigenstates as

$$|\psi(t)\rangle = \sum_n a_n(t)|\phi_n(t)\rangle, \tag{A2}$$

with $H(t)|\phi_n(t)\rangle = E_n(t)|\phi_n(t)\rangle$. Thus, the Schrödinger equation can be represented as (by left multiplying $\langle\phi_m(t)|$ on both sides)

$$i\frac{\partial a_m(t)}{\partial t} + i\sum_n a_n(t)\langle\phi_m(t)|\frac{\partial}{\partial t}|\phi_n(t)\rangle = E_m(t)a_m(t). \tag{A3}$$

We now make the gauge transformation $a_n(t) = \alpha_n(t)\exp[-i\omega_n(t)]\exp[i\gamma_n(t)]$, where the dynamic phase is defined as $\omega_n(t) \equiv -\int_t^{t_f} E_n(\tau)d\tau$, and the Berry phase is defined as $\gamma_n(t) = -i\int_t^{t_f}\langle n|\frac{\partial}{\partial t'}|n\rangle dt'$. As a result, we obtain (the indices $m \leftrightarrow n$ are exchanged)

$$\frac{\partial\alpha_n(t)}{\partial t} = -\sum_{m\neq n}\alpha_m(t)\langle\phi_n(t)|\frac{\partial}{\partial t}|\phi_m(t)\rangle \times \exp\{i[\omega_{nm}(t) - \gamma_{nm}(t)]\}, \tag{A4}$$

where $\omega_{nm}(t) = \omega_n(t) - \omega_m(t)$ and $\gamma_{nm}(t) = \gamma_n(t) - \gamma_m(t)$. Alternatively, we can write it in the integral form as follows:

$$\alpha_n(t) = -\int_{t_i}^{t} dt'\sum_{m\neq n}\alpha_m(t')\langle\phi_n(t')|\frac{\partial}{\partial t'}|\phi_m(t')\rangle \times \exp\{i[\omega_{nm}(t') - \gamma_{nm}(t')]\}. \tag{A5}$$

Now if the initial state is in the ground state, namely, $\alpha_0(0) = 1$ and $\alpha_m(0) = 0$ for $m \neq 0$, by making the adiabatic perturbation approximation [19,21], we obtain

$$\alpha_n(t) \approx -\int_{t_i}^{t} dt'\langle\phi_n(t')|\frac{\partial}{\partial t'}|\phi_0(t')\rangle \times \exp\{i[\omega_{n0}(t') - \gamma_{n0}(t')]\}. \tag{A6}$$

Using integration by parts, we obtain that

$$\alpha_n(t_f) \approx \left[i\frac{\langle\phi_n(t)|\frac{\partial}{\partial t}|\phi_0(t)\rangle}{E_n(t) - E_0(t)} - \frac{1}{E_n(t) - E_0(t)}\frac{d}{dt}\frac{\langle\phi_n(t)|\frac{\partial}{\partial t}|\phi_0(t)\rangle}{E_n(t) - E_0(t)} + \cdots\right] \times \exp\{i[\omega_{n0}(t) - \gamma_{n0}(t)]\}|_{t_i}^{t_f}. \tag{A7}$$

Since the time dependence of the Hamiltonian is usually introduced through the time-varying parameter, namely, $H(t) \equiv H[\lambda(t)]$, we have the following relation:

$$\langle\phi_n(t)|\frac{\partial}{\partial t}|\phi_0(t)\rangle = \frac{\partial\lambda}{\partial t}\langle\phi_n(\lambda)|\frac{\partial}{\partial\lambda}|\phi_0(\lambda)\rangle, \tag{A8}$$

while $\omega_n(\lambda) \equiv -\int_\lambda^{\lambda_f}\frac{E_n(\lambda')}{v(\lambda')}d\lambda'$, with $v(\lambda) = \frac{d\lambda}{dt}$, and $\gamma_n(\lambda) = -i\int_\lambda^{\lambda_f}\langle n|\frac{\partial}{\partial\lambda'}|n\rangle d\lambda'$. Therefore, the integral above can be rewritten as follows:

$$\alpha_n(\lambda_f) \approx \left[i\frac{\partial\lambda}{\partial t}\frac{\langle\phi_n(\lambda)|\frac{\partial}{\partial\lambda}|\phi_0(\lambda)\rangle}{E_n(\lambda)-E_0(\lambda)} - \frac{\partial^2\lambda}{\partial t^2}\frac{\langle\phi_n(\lambda)|\frac{\partial}{\partial\lambda}|\phi_0(\lambda)\rangle}{[E_n(\lambda)-E_0(\lambda)]^2} - \left(\frac{\partial\lambda}{\partial t}\right)^2\frac{1}{E_n(\lambda)-E_0(\lambda)}\frac{d}{d\lambda}\frac{\langle\phi_n(\lambda)|\frac{\partial}{\partial\lambda}|\phi_0(\lambda)\rangle}{E_n(\lambda)-E_0(\lambda)} + \ldots \right] \times \exp\{i[\omega_{n0}(\lambda)-\gamma_{n0}(\lambda)]\}|_{\lambda_i}^{\lambda_f}. \tag{A9}$$

When the quench is near adiabatic ($\frac{\partial\lambda}{\partial t} \to 0$), the transition amplitude can be approximated as

$$\alpha_n(\lambda_f) \approx i\frac{\partial\lambda}{\partial t}\frac{\langle\phi_n(\lambda)|\frac{\partial}{\partial\lambda}|\phi_0(\lambda)\rangle}{E_n(\lambda)-E_0(\lambda)} \times \exp\{i[\omega_{n0}(\lambda)-\gamma_{n0}(\lambda)]\}\Big|_{\lambda_i}^{\lambda_f}. \tag{A10}$$

Particularly, when the energy gap is large or the quench velocity is vanishing at the initial time, we have

$$a_n(\lambda_f) = \alpha_n(\lambda_f)\exp[-i\omega_n(\lambda_f)]\exp[i\gamma_n(\lambda_f)] \approx i\frac{\partial\lambda}{\partial t}\frac{\langle\phi_n(\lambda)|\frac{\partial}{\partial\lambda}|\phi_0(\lambda)\rangle}{E_n(\lambda)-E_0(\lambda)}\Big|_{\lambda_f}. \tag{A11}$$

This is the result presented in Ref. [18]. We can also utilize the following relation:

$$\langle\phi_n(\lambda)|\frac{\partial}{\partial\lambda}|\phi_m(\lambda)\rangle = -\frac{\langle\phi_n(\lambda)|\frac{\partial H}{\partial\lambda}|\phi_m(\lambda)\rangle}{E_n(\lambda)-E_m(\lambda)}. \tag{A12}$$

Thus, we have the response signal along the μ direction as a function of the quench velocity $v_\lambda \equiv \frac{\partial\lambda}{\partial t}$ up to the leading order as follows:

$$M_\mu \equiv -\langle\psi(t_f)|\frac{\partial H}{\partial\mu}|\psi(t_f)\rangle \approx -\langle\phi_0|\frac{\partial H}{\partial\mu}|\phi_0\rangle + i\frac{\partial\lambda}{\partial t}\sum_{n\neq 0}\frac{\langle\phi_0|\frac{\partial H}{\partial\mu}|\phi_n\rangle\langle\phi_n|\frac{\partial H}{\partial\lambda}|\phi_0\rangle - \mu\leftrightarrow\lambda}{[E_n(\lambda)-E_0(\lambda)]^2}\Big|_{\lambda_f}. \tag{A13}$$

This leads to the general formula of the quantum response as follows:

$$M_\mu = \text{const.} + v_\lambda\mathcal{F}_{\mu\lambda}^{(0)} + \mathcal{O}(v_\lambda^2), \tag{A14}$$

where the Berry curvature is given by

$$\mathcal{F}_{\mu\lambda}^{(m)} = i\sum_{n\neq m}\frac{\langle\phi_m|\frac{\partial H}{\partial\mu}|\phi_n\rangle\langle\phi_n|\frac{\partial H}{\partial\lambda}|\phi_m\rangle - \mu\leftrightarrow\lambda}{[E_n(\lambda)-E_m(\lambda)]^2}. \tag{A15}$$

APPENDIX B: EXACT EIGENVALUES AND EIGENVECTORS OF A 3 × 3 HERMITIAN MATRIX

In this section, we provide the analytic solution of the eigenvalues and eigenvectors of a general 3×3 Hermitian matrix represented as follows:

$$H = \begin{pmatrix} a_{11} & a_{12} & a_{13} \\ a_{12}^* & a_{22} & a_{23} \\ a_{13}^* & a_{23}^* & a_{33} \end{pmatrix}. \tag{B1}$$

The secular equation to calculate the eigenvalue is

$$\det(H-\lambda\mathbf{1}) = 0, \tag{B2}$$

which according to the Cayley-Hamilton theorem, corresponds to the cubic equation:

$$\lambda^3 - \text{Tr}(H)\lambda^2 - \tfrac{1}{2}\{\text{Tr}(H^2)-[\text{Tr}(H)]^2\}\lambda - \det(H) = 0. \tag{B3}$$

Since H is a Hermitian operator, $\text{Tr}(H^2)$, $\text{Tr}(H)$, and $\det(H)$ are all real quantities. To further simplify the corresponding cubic equation, we now make some transformations as follows:

$$B = H - \frac{\text{Tr}[H]}{3}\mathbf{1}, \qquad A = \sqrt{\frac{2}{\text{Tr}[B^2]}}B. \tag{B4}$$

As a result, the eigenvalues of H and the eigenvalues of A follow the relation:

$$\lambda_k = \sqrt{\frac{\text{Tr}[B^2]}{2}}t_k + \frac{\text{Tr}[H]}{3}. \tag{B5}$$

We notice that $\text{Tr}[A] = 0$ and $\text{Tr}[A^2] = 2$. Consequently, the secular equation to calculate the eigenvalues of A becomes a depressed cubic equation:

$$t^3 - t - q = 0, \tag{B6}$$

with $q = \det(A)$. Since the operator A is still a Hermitian operator, all the eigenvalues are real, then we can assume the solution to be $t = u\cos\theta$. We can prove that $-\frac{2}{3\sqrt{3}} < q < \frac{2}{3\sqrt{3}}$, when Eq. (B6) has three distinct real roots (it is easy to observe by plotting the graph of the function). Specifically, when $q = \frac{2}{3\sqrt{3}}$, two multiple roots correspond to the stationary point of $f(t) = t^3 - t$, namely, $t_1 = t_2 = \frac{1}{\sqrt{3}}$ and $t_3 = -\frac{2}{\sqrt{3}}$. It is similar when $q = -\frac{2}{3\sqrt{3}}$, and we can conclude that $-\frac{2}{\sqrt{3}} \leqslant t \leqslant \frac{2}{\sqrt{3}}$. As a result, we can choose $u = \frac{2}{\sqrt{3}}$. After dividing the

equation by $u^3/4$, the depressed cubic equation in Eq. (B6) now becomes

$$4\cos^3\theta - 3\cos\theta - \tfrac{3}{2}\sqrt{3}q = 0. \tag{B7}$$

Using the trigonometric identity:

$$4\cos^3\theta - 3\cos\theta = \cos(3\theta), \tag{B8}$$

we obtain that

$$\cos(3\theta) = \tfrac{3}{2}\sqrt{3}q. \tag{B9}$$

As a result, we have the three eigenvalues of matrix A as follows:

$$t_k = \frac{2}{\sqrt{3}}\cos\left\{\frac{1}{3}\arccos\left[\frac{3}{2}\sqrt{3}\det(A)\right] - \frac{2\pi k}{3}\right\}, \tag{B10}$$

for $k = 0, 1, 2$. Then the eigenvalues of H can be determined by Eq. (B5).

The eigenstates of the 3×3 Hermitian matrix H can be represented as the cross-product of two three-dimensional vectors $|\tilde{\Psi}_m\rangle = [(\mathbf{h}_1 - E_m\mathbf{e}_1) \times (\mathbf{h}_3 - E_m\mathbf{e}_3)]^*$ if the two vectors are linear independent [72]. Here, $\mathbf{h}_j$ is the jth column of the Hermitian matrix H, and $\mathbf{e}_i$ is the unit vector, like $\mathbf{e}_1 = (1, 0, 0)^{\mathrm{T}}$. We now make a brief proof to show that $|\tilde{\Psi}_m\rangle$ is indeed the eigenstate. First, if $|\tilde{\Psi}_m\rangle$ is the eigenstate, then we have $(H - E_m\mathbf{1})|\tilde{\Psi}_m\rangle = 0$, or equivalently, we must prove that

$$\langle\tilde{\Psi}_m|(H - E_m\mathbf{1})|\psi\rangle = 0, \tag{B11}$$

where $|\psi\rangle = \alpha_1\mathbf{e}_1 + \alpha_2\mathbf{e}_2 + \alpha_3\mathbf{e}_3$ is an arbitrary wave vector. After the expansion, we have

$$\begin{aligned}&\langle\tilde{\Psi}_m|(H - E_m\mathbf{1})|\psi\rangle \\ &= \alpha_1\langle\tilde{\Psi}_m|(\mathbf{h}_1 - E_m\mathbf{e}_1)\rangle + \alpha_2\langle\tilde{\Psi}_m|(\mathbf{h}_2 - E_m\mathbf{e}_2)\rangle \\ &\quad + \alpha_3\langle\tilde{\Psi}_m|(\mathbf{h}_3 - E_m\mathbf{e}_3)\rangle.\end{aligned} \tag{B12}$$

Obviously, both the first and last terms equal zero. To prove the second term equals zero, we need to utilize the property of the mixed product as follows:

$$(\mathbf{a} \times \mathbf{b}) \cdot \mathbf{c} = \det\begin{pmatrix} a_1 & b_1 & c_1 \\ a_2 & b_2 & c_2 \\ a_3 & b_3 & c_3 \end{pmatrix}. \tag{B13}$$

As a result, we can prove that

$$\begin{aligned}&\langle\tilde{\Psi}_m|(\mathbf{h}_2 - E_m\mathbf{e}_2)\rangle \\ &= [(\mathbf{h}_1 - E_m\mathbf{e}_1) \times (\mathbf{h}_3 - E_m\mathbf{e}_3)] \cdot (\mathbf{h}_2 - E_m\mathbf{e}_2) \\ &= \det(H - E_m\mathbf{1}) = 0.\end{aligned}$$

When these two vectors are linear dependent, namely, $(\mathbf{h}_1 - E_m\mathbf{e}_1) = \mu(\mathbf{h}_3 - E_m\mathbf{e}_3)$, the eigenstate can be straightforwardly calculated by solving $(H - E_m\mathbf{1})|\tilde{\Psi}_m\rangle = 0$, and the normalized eigenstate is given by

$$|\Psi_m\rangle = \frac{1}{1 + |\mu|^2}\begin{pmatrix} 1 \\ 0 \\ -\mu \end{pmatrix}. \tag{B14}$$

For instance, this is the situation when $\theta = \pi/2$ in the Hamiltonian [Eq. (18)] in the main text, where for $E_2 = D$, the corresponding eigenstate can be determined using the above expression.

APPENDIX C: APPROXIMATE ANALYTIC RESULT OF THE BERRY CURVATURE

By plotting the Berry curvature under various NV parameters in Fig. 2, we observe that the susceptibility of the Berry curvature exhibits divergent behavior when $D \sim 1$ and $\theta \sim 0$. This suggests that a slight change in the parameter values can lead to a significant variation in the response signal. Consequently, selecting $D = 1$ and $\theta = 0$ as the work point allows us to achieve the maximum signal contrast. To facilitate the application of the quantum response-based sensing scheme, we can make approximations to Eq. (23) near the work point, leading to a much simpler analytic expression for the Berry curvature.

Near the work point, the energy level E_1 is nearly degenerate with the energy level E_2. Thus, we can neglect the term involving $(E_1 - E_3)^2$ in the denominator in Eq. (10). As a result, the Berry curvature in Eq. (23) can be well approximated by only the first term:

$$\begin{aligned}\mathcal{F}^{(1)}_{\phi\theta} &\approx \frac{9\sqrt{3}\sin\theta}{8(D^2+3)^{5/2}\sin(\varphi)} \\ &\quad \times \left\{\frac{E_3[D\cos(2\theta) + 3D - 2E_3]}{\sin^2\left(\frac{\varphi}{3}\right)}\right\}.\end{aligned} \tag{C1}$$

Since $\theta \sim 0$, by substituting $\sin\theta \approx \theta$ and $\cos 2\theta \approx 1$, we obtain

$$\mathcal{F}^{(1)}_{\phi\theta} \approx \frac{9\sqrt{3}\theta}{8(D^2+3)^{5/2}\sin(\varphi)}\left\{\frac{E_3[D + 3D - 2E_3]}{\sin^2\left(\frac{\varphi}{3}\right)}\right\}. \tag{C2}$$

Moreover, the eigenenergy E_3 in Eq. (19) can be approximated as $E_3 \approx 2 + (D - 1)$; thus, we obtain

$$\mathcal{F}^{(1)}_{\phi\theta} \approx \frac{9\sqrt{3}\theta(D^2-1)}{4(D^2+3)^{5/2}\sin\varphi}\frac{1}{\sin^2\frac{\varphi}{3}}. \tag{C3}$$

By substituting $\cos^2\theta \approx 1 - \theta^2$ in Eq. (20), we obtain

$$\cos\varphi = \frac{D(18 - 2D^2 - 27\theta^2)}{2\sqrt{(D^2+3)^3}}. \tag{C4}$$

Now we denote $\mathcal{F}^{(1)}_{\phi\theta} \approx f_1 f_2$, with

$$\begin{aligned}f_1 &= \frac{9\sqrt{3}\theta(D^2-1)}{4(D^2+3)^{5/2}\sin\varphi} \\ &= \frac{9\sqrt{3}\theta(D^2-1)}{4(D^2+3)^{5/2}\sqrt{1 - \frac{D^2(18-2D^2-27\theta^2)^2}{4(D^2+3)^3}}}.\end{aligned} \tag{C5}$$

By performing a series expansion near $D = 1$, we obtain

$$f_1 = \frac{3(D-1)}{4\sqrt{32 - 27\theta^2}} + \mathcal{O}[D-1]^2 \cong \frac{3(D-1)}{16\sqrt{2}}, \tag{C6}$$

where the θ^2 term has been neglected in the last line. Moreover, by applying a series expansion of Eq. (C4) near $D = 1$, we obtain

$$\begin{aligned}\cos\varphi &= \frac{1}{256}(16 - 27\theta^2) \\ &\quad + \frac{27}{512}\theta^2(-16 + 27\theta^2)(D-1) + \mathcal{O}[D-1]^2\end{aligned}$$

$$\cong \frac{1}{256}(16-27\theta^2)^2$$
$$\cong 1-\frac{27\theta^2}{8}. \tag{C7}$$

As a result,

$$f_2 = \frac{1}{\sin^2\frac{\varphi}{3}} \approx \frac{1}{\sin^2\left[\frac{1}{3}\arccos\left(1-\frac{27\theta^2}{8}\right)\right]}, \tag{C8}$$

and by performing a series expansion near $\theta = 0$, we obtain

$$f_2 \cong \frac{8}{3\theta^2} - \frac{5}{12} - \frac{13\theta^2}{128} + \mathcal{O}[\theta]^3$$
$$\cong \frac{8}{3\theta^2} - \frac{5}{12}. \tag{C9}$$

Finally, we obtain the approximate analytic expression of the Berry curvature near $D = 1$ and $\theta = 0$ as follows:

$$\mathcal{F}^{(1)}_{\phi\theta} = f_1 f_2 \approx \left(\frac{1}{\theta^2} - \frac{5}{32}\right)\frac{D-1}{2\sqrt{2}}. \tag{C10}$$

This result immediately indicates that

$$\lim_{\theta\to 0}\left.\frac{\partial \mathcal{F}^{(1)}_{\phi\theta}}{\partial D}\right|_{D=1} \to \infty. \tag{C11}$$

APPENDIX D: EXPLANATION OF OSCILLATIONS IN THE RESPONSE SIGNAL

In this section, we provide explanations for the oscillations observed in the quantum response signal depicted in Figs. 3–5. For simplicity, but without loss of generality, we consider the case where the rotating quench field is applied to a single qubit. Since the zero-field splitting term vanishes for a spin-$\frac{1}{2}$ system, the Hamiltonian can be written as

$$H(t) = \exp[-i\phi(t)S_z]\exp[-i\theta(t)S_y]S_z \times \exp[i\theta(t)S_y]\exp[i\phi(t)S_z], \tag{D1}$$

where $S_{x,y,z}$ are spin operators for the qubit. The instantaneous ground state of this Hamiltonian is given by

$$|\Psi\rangle = \exp(-i\phi S_z)\exp(-i\theta S_y)|\downarrow\rangle. \tag{D2}$$

We can straightforwardly calculate the Berry curvature using the formula in Eq. (2) as

$$\mathcal{F}_{\phi\theta}(\phi,\theta) = \sin\theta. \tag{D3}$$

Like the rotating quench scheme utilizing NV centers in the main text, here, we apply the same rotating quench field described by $\phi(t) = 0$ and $\theta(t) = \frac{v^2t^2}{2\pi}$. In Fig. 8(a), we also calculate the quantum response signal for the single qubit driven by this rotating quench field. Again, the solid line corresponds to $\langle S_y\rangle \equiv \langle\psi(t_f)|S_y|\psi(t_f)\rangle$ as a function of the quench velocity $v_\theta(t_f) = v$, where $|\psi(t_f)\rangle = \mathcal{T}\exp[i\int_0^{t_f} H(t')dt']|\downarrow\rangle$ with $t_f = \pi/v$. Meanwhile, the dashed line corresponds to the analytic result $v\mathcal{F}_{\phi\theta}(\phi = 0, \theta = \pi/2)$.

Upon comparing Figs. 3 and 8(a), it is evident that the calculated quantum response signals exhibit several consistent characteristics: (i) As the quench velocity approaches zero, the exactly calculated quantum response signal closely aligns with the analytic result (the Berry curvature multiplied by the quench velocity); (ii) oscillations gradually manifest as a function of the quench velocity; and (iii) the amplitude of these oscillations grows with increasing quench velocity.

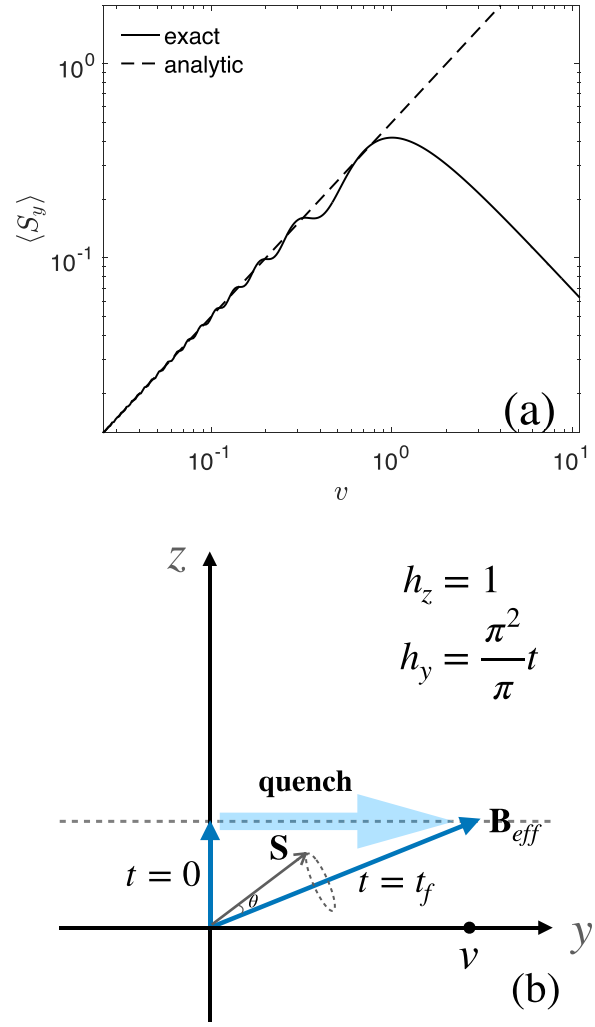

FIG. 8. Explanation of the oscillations in the quantum response signal. (a) Quantum response signal driven by a rotating quench field for a single qubit. The solid line corresponds to the exact numerical calculation of the dynamics, while the dashed line represents the analytic result obtained by multiplying the Berry curvature by the quench velocity. (b) Schematic plot illustrating the motion of the spin vector **S** as it precesses about the effective magnetic field $\mathbf{B}_{\text{eff}}$ in the rotating reference frame. The relative angle θ between the spin vector and the effective magnetic field varies with the quench velocity.

The first characteristic can be explained by the quantum response theory, while the explanation of the second and third characteristics requires the employment of the rotating reference frame. By making a unitary transformation, we obtain the effective Hamiltonian in the rotating reference frame as follows:

$$H_{\text{eff}} = \exp[i\theta(t)S_y]H(t)\exp[-i\theta(t)S_y]$$
$$= S_z + \frac{v^2}{\pi}tS_y = h_zS_z + h_yS_y. \tag{D4}$$

This effective magnetic field $\mathbf{B}_{\text{eff}} = (0, h_y, h_z)$ is illustrated in Fig. 8. In the rotating reference frame defined by the rotation about the y axis, the spin vector will adiabatically follow the linearly changing instantaneous magnetic field while simultaneously precessing about it (see Ref. [70]). The precession angle between the spin vector and the instantaneous effective magnetic field in the rotating frame is determined by the quench velocity [70]. As the quench velocity increases, the precession angle also increases. Conversely, when the quench velocity approaches zero, this angle tends toward zero as well. In this limit, the spin vector adiabatically follows the time-varying effective magnetic field in the rotating reference frame, resulting in a slight change in the projection of the spin vector along the y axis. This subtle variation indicates a small oscillation when the quench velocity is small. In contrast, for a finite quench velocity, the relative angle between the spin vector and the effective magnetic field remains finite, signifying a notable alteration in the projection of the spin vector along the y axis. This elucidates why the amplitude of the oscillation increases with the quench velocity.

APPENDIX E: RAMSEY SENSING PROTOCOL IN THE PRESENCE OF DECOHERENCE

For simplicity, here, we consider the Ramsey sensing scheme for a single qubit in the presence of decoherence. Similar Ramsey sensing schemes can also be applied to NV centers. The Hamiltonian describing the sensor qubit in the presence of decoherence, arising from coupling to surrounding spins, is given by

$$H = h_0 S_z + A \sum_{k=1}^{N} \mathbf{S} \cdot \mathbf{I}_k. \tag{E1}$$

This Hamiltonian also describes the homogeneous central spin model [53], where $\mathbf{S} = (S_x, S_y, S_z)$ represents the spin operator of the central electronic spin (or qubit), $\mathbf{I}_k$ denotes the spin operator of the kth nuclear spin (assuming $I_k = \frac{1}{2}$), and A represents the hyperfine coupling strength. In the Ramsey sensing scheme, the interaction between the central electronic spin and the surrounding nuclear spins introduces decoherence during the parameter encoding process, leading to reduction of the overall sensitivity.

For the standard Ramsey sensing scheme, the initial state of the central spin is prepared as

$$|\phi(0)\rangle = \frac{1}{\sqrt{2}}(|\uparrow\rangle + |\downarrow\rangle), \tag{E2}$$

while the initial state of the kth nuclear spin is given by the thermal state:

$$\rho_{nk} = \begin{pmatrix} \frac{1+P}{2} & 0 \\ 0 & \frac{1-P}{2} \end{pmatrix}. \tag{E3}$$

Here, P represents the nuclear polarization. Thus, the initial state of the compound system is given by

$$\rho(0) = |\phi(0)\rangle\langle\phi(0)| \otimes \rho_n, \tag{E4}$$

where $\rho_n = \otimes_{k=1}^{N} \rho_{nk}$. To investigate the Ramsey sensing scheme, we need to calculate the dynamics of the compound system:

$$\rho(t) = \exp(-iHt)\rho(0)\exp(iHt). \tag{E5}$$

Finally, we measure the expectation value of the central spin $\langle S_x(t)\rangle = \text{Tr}[\rho(t)S_x]$ to estimate the magnitude of the magnetic field h_0.

In fact, for the specific initial state of the nuclear spins as given in Eq. (E3), the dynamics of the compound system can be exactly calculated as follows:

$$\rho(t) = \sum_{I_0=k}^{N/2} \sum_{M_0=-I_0}^{I_0} \omega(I_0, M_0)|\psi(t)\rangle\langle\psi(t)|, \tag{E6}$$

where $|\psi(t)\rangle = \exp(-iHt)|\phi(0)\rangle \otimes |I_0, M_0\rangle$. Here, the weight function is given by

$$\omega(I_0, M_0) = C_N^{(N/2)-I_0} \left(\frac{1+P}{2}\right)^{(N/2)-M_0} \times \left(\frac{1-P}{2}\right)^{(N/2)+M_0} \frac{2I_0+1}{\frac{N}{2}+I_0+1}, \tag{E7}$$

where $|I_0, M_0\rangle$ represents the eigenstate of the collective nuclear spin operator $\mathbf{I} = \sum_{k=1}^{N} \mathbf{I}_k$. Accordingly, the spin expectation value is given by

$$\langle S_x(t)\rangle = \sum_{I_0=k}^{N/2} \sum_{M_0=-I_0}^{I_0} \omega(I_0, M_0)\langle\psi(t)|S_x|\psi(t)\rangle. \tag{E8}$$

Since $J_z = S_z + I_z$ is a conserved quantity, we can exactly obtain [73]

$$\langle\psi(t)|S_x|\psi(t)\rangle = \frac{1}{2}\left[\cos(h_1 t)\cos(h_2 t) + \frac{h_{1z}h_{2z}}{h_1 h_2}\sin(h_1 t)\sin(h_2 t)\right], \tag{E9}$$

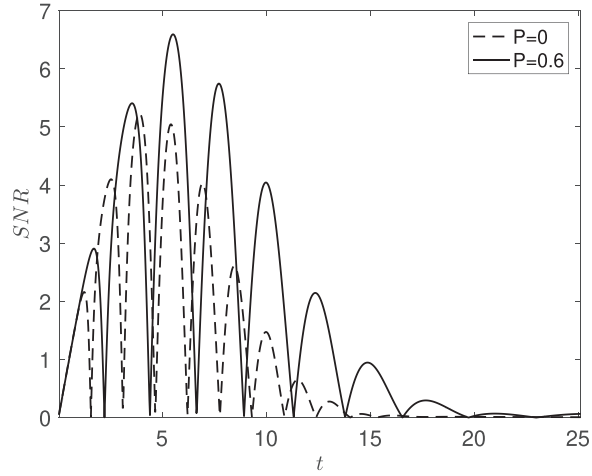

FIG. 9. Time evolution of the signal-to-noise ratio under different nuclear polarizations for the Ramsey sensing scheme. The parameters for the calculation are fixed as follows: $h_0 = 2$, $N = 20$, and $A = 0.1$.

where

$$h_{1x} = \frac{A}{2}\sqrt{(I_0 - M_0)(I_0 + M_0 + 1)},$$
$$h_{1z} = \frac{1}{2}\left(h_0 + AM_0 + \frac{A}{2}\right),$$
$$h_{2x} = \frac{A}{2}\sqrt{(I_0 + M_0)(I_0 - M_0 + 1)},$$
$$h_{2z} = \frac{1}{2}\left(-h_0 - AM_0 + \frac{A}{2}\right),$$
$$h_1 = \sqrt{h_{1x}^2 + h_{1z}^2}, \quad h_2 = \sqrt{h_{2x}^2 + h_{2z}^2}. \tag{E10}$$

To quantitatively investigate the impact of decoherence on the sensitivity of the Ramsey sensing scheme, we calculate the signal-to-noise ratio (SNR) using the error propagation formula:

$$\mathrm{SNR} = \frac{\left|\frac{\partial\langle S_x(t)\rangle}{\partial h_0}\right|}{\sqrt{\frac{1}{4} - \langle S_x(t)\rangle^2}}. \tag{E11}$$

Typically, a larger SNR indicates higher sensitivity in the experiment. In Fig. 9, we plot the SNR as a function of evolution time with different nuclear polarizations. This figure illustrates that the SNR evolves periodically, with local maxima occurring when $\langle S_x\rangle \sim 0$, indicating a regime suitable for slope detection. Meanwhile, owing to the presence of decoherence, there exists a global optimal sensing time to achieve the global maximal SNR. It is evident that, with increasing nuclear polarization, the maximal SNR also increases. This is because increasing the nuclear polarization extends the coherence time, thereby enhancing the precision of magnetic field sensing.

[1] S. L. Braunstein and C. M. Caves, Statistical distance and the geometry of quantum states, Phys. Rev. Lett. **72**, 3439 (1994).

[2] V. Giovannetti, S. Lloyd, and L. Maccone, Quantum metrology, Phys. Rev. Lett. **96**, 010401 (2006).

[3] V. Giovannetti, S. Lloyd, and L. Maccone, Advances in quantum metrology, Nat. Photon. **5**, 222 (2011).

[4] B. Escher, R. de Matos Filho, and L. Davidovich, General framework for estimating the ultimate precision limit in noisy quantum-enhanced metrology, Nat. Phys. **7**, 406 (2011).

[5] L. Pezzè, A. Smerzi, M. K. Oberthaler, R. Schmied, and P. Treutlein, Quantum metrology with nonclassical states of atomic ensembles, Rev. Mod. Phys. **90**, 035005 (2018).

[6] D. Braun, G. Adesso, F. Benatti, R. Floreanini, U. Marzolino, M. W. Mitchell, and S. Pirandola, Quantum-enhanced measurements without entanglement, Rev. Mod. Phys. **90**, 035006 (2018).

[7] C. L. Degen, F. Reinhard, and P. Cappellaro, Quantum sensing, Rev. Mod. Phys. **89**, 035002 (2017).

[8] J. F. Barry, J. M. Schloss, E. Bauch, M. J. Turner, C. A. Hart, L. M. Pham, and R. L. Walsworth, Sensitivity optimization for NV-diamond magnetometry, Rev. Mod. Phys. **92**, 015004 (2020).

[9] J. Du, F. Shi, X. Kong, F. Jelezko, and J. Wrachtrup, Single-molecule scale magnetic resonance spectroscopy using quantum diamond sensors, Rev. Mod. Phys. **96**, 025001 (2024).

[10] B. Yurke, S. L. McCall, and J. R. Klauder, SU(2) and SU(1,1) interferometers, Phys. Rev. A **33**, 4033 (1986).

[11] G. Wang, Y.-X. Liu, J. M. Schloss, S. T. Alsid, D. A. Braje, and P. Cappellaro, Sensing of arbitrary-frequency fields using a quantum mixer, Phys. Rev. X **12**, 021061 (2022).

[12] D. Maclaurin, L. Hall, A. Martin, and L. Hollenberg, Nanoscale magnetometry through quantum control of nitrogen-vacancy centres in rotationally diffusing nanodiamonds, New J. Phys. **15**, 013041 (2013).

[13] J. C. Budich and E. J. Bergholtz, Non-Hermitian topological sensors, Phys. Rev. Lett. **125**, 180403 (2020).

[14] J. Wiersig, Review of exceptional point-based sensors, Photon. Res. **8**, 1457 (2020).

[15] Y. Chu, Y. Liu, H. Liu, and J. Cai, Quantum sensing with a single-qubit pseudo-Hermitian system, Phys. Rev. Lett. **124**, 020501 (2020).

[16] U. Mishra and A. Bayat, Driving enhanced quantum sensing in partially accessible many-body systems, Phys. Rev. Lett. **127**, 080504 (2021).

[17] W. Ding, Y. Liu, Z. Zheng, and S. Chen, Dynamic quantum-enhanced sensing without entanglement in central spin systems, Phys. Rev. A **106**, 012604 (2022).

[18] V. Gritsev and A. Polkovnikov, Dynamical quantum Hall effect in the parameter space, Proc. Natl. Acad. Sci. **109**, 6457 (2012).

[19] G. Rigolin, G. Ortiz, and V. H. Ponce, Beyond the quantum adiabatic approximation: Adiabatic perturbation theory, Phys. Rev. A **78**, 052508 (2008).

[20] J. E. Avron, M. Fraas, G. M. Graf, and O. Kenneth, Quantum response of dephasing open systems, New J. Phys. **13**, 053042 (2011).

[21] C. De Grandi and A. Polkovnikov, Adiabatic perturbation theory: From Landau-Zener problem to quenching through a quantum critical point, in *Quantum Quenching, Annealing and Computation* (Springer, Berlin, 2010), pp. 75–114.

[22] C. De Grandi, A. Polkovnikov, and A. Sandvik, Microscopic theory of non-adiabatic response in real and imaginary time, J. Phys.: Condens. Matter **25**, 404216 (2013).

[23] M. W. Doherty, F. Dolde, H. Fedder, F. Jelezko, J. Wrachtrup, N. B. Manson, and L. C. L. Hollenberg, Theory of the ground-state spin of the NV^- center in diamond, Phys. Rev. B **85**, 205203 (2012).

[24] M. W. Doherty, N. B. Manson, P. Delaney, F. Jelezko, J. Wrachtrup, and L. C. Hollenberg, The nitrogen-vacancy colour centre in diamond, Phys. Rep. **528**, 1 (2013).

[25] G. Balasubramanian, P. Neumann, D. Twitchen, M. Markham, R. Kolesov, N. Mizuochi, J. Isoya, J. Achard, J. Beck, J. Tissler *et al.*, Ultralong spin coherence time in isotopically engineered diamond, Nat. Mater. **8**, 383 (2009).

[26] R. Hanson, V. Dobrovitski, A. Feiguin, O. Gywat, and D. Awschalom, Coherent dynamics of a single spin interacting with an adjustable spin bath, Science **320**, 352 (2008).

[27] A. A. Wood, A. G. Aeppli, E. Lilette, Y. Y. Fein, A. Stacey, L. C. L. Hollenberg, R. E. Scholten, and A. M. Martin, T_2-limited sensing of static magnetic fields via fast rotation of quantum spins, Phys. Rev. B **98**, 174114 (2018).

[28] Y.-X. Liu, A. Ajoy, and P. Cappellaro, Nanoscale vector dc magnetometry via ancilla-assisted frequency up-conversion, Phys. Rev. Lett. **122**, 100501 (2019).

[29] A. Ajoy, U. Bissbort, M. D. Lukin, R. L. Walsworth, and P. Cappellaro, Atomic-scale nuclear spin imaging using quantum-assisted sensors in diamond, Phys. Rev. X **5**, 011001 (2015).

[30] H. Mamin, M. Kim, M. Sherwood, C. Rettner, K. Ohno, D. Awschalom, and D. Rugar, Nanoscale nuclear magnetic resonance with a nitrogen-vacancy spin sensor, Science **339**, 557 (2013).

[31] M. S. Grinolds, S. Hong, P. Maletinsky, L. Luan, M. D. Lukin, R. L. Walsworth, and A. Yacoby, Nanoscale magnetic imaging of a single electron spin under ambient conditions, Nat. Phys. **9**, 215 (2013).

[32] V. M. Acosta, E. Bauch, M. P. Ledbetter, C. Santori, K.-M. C. Fu, P. E. Barclay, R. G. Beausoleil, H. Linget, J. F. Roch, F. Treussart *et al.*, Diamonds with a high density of nitrogen-vacancy centers for magnetometry applications, Phys. Rev. B **80**, 115202 (2009).

[33] J. R. Maze, P. L. Stanwix, J. S. Hodges, S. Hong, J. M. Taylor, P. Cappellaro, L. Jiang, M. G. Dutt, E. Togan, A. Zibrov *et al.*, Nanoscale magnetic sensing with an individual electronic spin in diamond, Nature (London) **455**, 644 (2008).

[34] C. Du, T. Van der Sar, T. X. Zhou, P. Upadhyaya, F. Casola, H. Zhang, M. C. Onbasli, C. A. Ross, R. L. Walsworth, Y. Tserkovnyak *et al.*, Control and local measurement of the spin chemical potential in a magnetic insulator, Science **357**, 195 (2017).

[35] A. Finco, A. Haykal, R. Tanos, F. Fabre, S. Chouaieb, W. Akhtar, I. Robert-Philip, W. Legrand, F. Ajejas, K. Bouzehouane *et al.*, Imaging non-collinear antiferromagnetic textures via single spin relaxometry, Nat. Commun. **12**, 767 (2021).

[36] A. Jenkins, M. Pelliccione, G. Yu, X. Ma, X. Li, K. L. Wang, and A. C. Bleszynski Jayich, Single-spin sensing of domain-wall structure and dynamics in a thin-film skyrmion host, Phys. Rev. Mater. **3**, 083801 (2019).

[37] A. O. Sushkov, I. Lovchinsky, N. Chisholm, R. L. Walsworth, H. Park, and M. D. Lukin, Magnetic resonance detection of individual proton spins using quantum reporters, Phys. Rev. Lett. **113**, 197601 (2014).

[38] H. Zhang, M. J. H. Ku, F. Casola, C. H. R. Du, T. van der Sar, M. C. Onbasli, C. A. Ross, Y. Tserkovnyak, A. Yacoby, and R. L. Walsworth, Spin-torque oscillation in a magnetic insulator probed by a single-spin sensor, Phys. Rev. B **102**, 024404 (2020).

[39] D. Maclaurin, M. W. Doherty, L. C. L. Hollenberg, and A. M. Martin, Measurable quantum geometric phase from a rotating single spin, Phys. Rev. Lett. **108**, 240403 (2012).

[40] M. Yu, P. Yang, M. Gong, Q. Cao, Q. Lu, H. Liu, S. Zhang, M. B. Plenio, F. Jelezko, T. Ozawa *et al.*, Experimental measurement of the quantum geometric tensor using coupled qubits in diamond, Natl. Sci. Rev. **7**, 254 (2020).

[41] M. P. Ledbetter, K. Jensen, R. Fischer, A. Jarmola, and D. Budker, Gyroscopes based on nitrogen-vacancy centers in diamond, Phys. Rev. A **86**, 052116 (2012).

[42] A. Ajoy and P. Cappellaro, Stable three-axis nuclear-spin gyroscope in diamond, Phys. Rev. A **86**, 062104 (2012).

[43] K. Arai, J. Lee, C. Belthangady, D. R. Glenn, H. Zhang, and R. L. Walsworth, Geometric phase magnetometry using a solid-state spin, Nat. Commun. **9**, 4996 (2018).

[44] G. Balasubramanian, A. Lazariev, S. R. Arumugam, and D.-w. Duan, Nitrogen-vacancy color center in diamond—Emerging nanoscale applications in bioimaging and biosensing, Curr. Opin. Chem. Biol. **20**, 69 (2014).

[45] J. Provost and G. Vallee, Riemannian structure on manifolds of quantum states, Commun. Math. Phys. **76**, 289 (1980).

[46] A. Tarantola, *Elements for Physics: Quantities, Qualities, and Intrinsic Theories* (Springer, Berlin, 2006).

[47] M. Chen, C. Meng, Q. Zhang, C. Duan, F. Shi, and J. Du, Quantum metrology with single spins in diamond under ambient conditions, Natl. Sci. Rev. **5**, 346 (2018).

[48] F. Dolde, H. Fedder, M. W. Doherty, T. Nöbauer, F. Rempp, G. Balasubramanian, T. Wolf, F. Reinhard, L. C. Hollenberg, F. Jelezko *et al.*, Electric-field sensing using single diamond spins, Nat. Phys. **7**, 459 (2011).

[49] A. B. Siddique and T. A. Khraishi, Eigenvalues and eigenvectors for 3×3 symmetric matrices: An analytical approach, J. Adv. Math. Comput. Sci. **35**, 106 (2020).

[50] O. K. Smith, Eigenvalues of a symmetric 3×3 matrix, Commun. ACM **4**, 168 (1961).

[51] W. Ding, A. Shi, J. Q. You, and W. Zhang, High-fidelity quantum memory utilizing inhomogeneous nuclear polarization in a quantum dot, Phys. Rev. B **90**, 235421 (2014).

[52] W. Zhang, V. V. Dobrovitski, K. A. Al-Hassanieh, E. Dagotto, and B. N. Harmon, Hyperfine interaction induced decoherence of electron spins in quantum dots, Phys. Rev. B **74**, 205313 (2006).

[53] W.-B. He, S. Chesi, H.-Q. Lin, and X.-W. Guan, Exact quantum dynamics of XXZ central spin problems, Phys. Rev. B **99**, 174308 (2019).

[54] R. Fischer, A. Jarmola, P. Kehayias, and D. Budker, Optical polarization of nuclear ensembles in diamond, Phys. Rev. B **87**, 125207 (2013).

[55] J. M. Schloss, J. F. Barry, M. J. Turner, and R. L. Walsworth, Simultaneous broadband vector magnetometry using solid-state spins, Phys. Rev. Appl. **10**, 034044 (2018).

[56] S.-Y. Lee, M. Niethammer, and J. Wrachtrup, Vector magnetometry based on $S = \frac{3}{2}$ electronic spins, Phys. Rev. B **92**, 115201 (2015).

[57] M. Niethammer, M. Widmann, S.-Y. Lee, P. Stenberg, O. Kordina, T. Ohshima, N. T. Son, E. Janzén, and J. Wrachtrup, Vector magnetometry using silicon vacancies in 4H-SiC under ambient conditions, Phys. Rev. Appl. **6**, 034001 (2016).

[58] H. Zheng, Z. Sun, G. Chatzidrosos, C. Zhang, K. Nakamura, H. Sumiya, T. Ohshima, J. Isoya, J. Wrachtrup, A. Wickenbrock, and D. Budker, Microwave-free vector magnetometry with nitrogen-vacancy centers along a single axis in diamond, Phys. Rev. Appl. **13**, 044023 (2020).

[59] N. Wang, G.-Q. Liu, W.-H. Leong, H. Zeng, X. Feng, S.-H. Li, F. Dolde, H. Fedder, J. Wrachtrup, X.-D. Cui, S. Yang, Q. Li, and R.-B. Liu, Magnetic criticality enhanced hybrid nanodiamond thermometer under ambient conditions, Phys. Rev. X **8**, 011042 (2018).

[60] L. Childress, M. Gurudev Dutt, J. Taylor, A. Zibrov, F. Jelezko, J. Wrachtrup, P. Hemmer, and M. Lukin, Coherent dynamics of

coupled electron and nuclear spin qubits in diamond, Science **314**, 281 (2006).

[61] J. M. Taylor, P. Cappellaro, L. Childress, L. Jiang, D. Budker, P. Hemmer, A. Yacoby, R. Walsworth, and M. Lukin, High-sensitivity diamond magnetometer with nanoscale resolution, Nat. Phys. **4**, 810 (2008).

[62] G. Q. Yan, S. Li, T. Yamamoto, M. Huang, N. J. Mclaughlin, T. Nozaki, H. Wang, S. Yuasa, and C. R. Du, Electric-field-induced coherent control of nitrogen-vacancy centers, Phys. Rev. Appl. **18**, 064031 (2022).

[63] J.-P. Tetienne, T. Hingant, J.-V. Kim, L. H. Diez, J.-P. Adam, K. Garcia, J.-F. Roch, S. Rohart, A. Thiaville, D. Ravelosona *et al.*, Nanoscale imaging and control of domain-wall hopping with a nitrogen-vacancy center microscope, Science **344**, 1366 (2014).

[64] E. M. Palmero, C. Bran, R. P. Del Real, and M. Vázquez, Vortex domain wall propagation in periodically modulated diameter FeCoCu nanowire as determined by the magneto-optical Kerr effect, Nanotechnology **26**, 461001 (2015).

[65] J. Gieseler, A. Kabcenell, E. Rosenfeld, J. D. Schaefer, A. Safira, M. J. A. Schuetz, C. Gonzalez-Ballestero, C. C. Rusconi, O. Romero-Isart, and M. D. Lukin, Single-spin magnetomechanics with levitated micromagnets, Phys. Rev. Lett. **124**, 163604 (2020).

[66] P. Huillery, T. Delord, L. Nicolas, M. Van Den Bossche, M. Perdriat, and G. Hétet, Spin mechanics with levitating ferromagnetic particles, Phys. Rev. B **101**, 134415 (2020).

[67] S. D. Bennett, S. Kolkowitz, Q. P. Unterreithmeier, P. Rabl, A. C. Bleszynski Jayich, J. G. E. Harris, and M. D. Lukin, Measuring mechanical motion with a single spin, New J. Phys. **14**, 125004 (2012).

[68] M. M. Rams, P. Sierant, O. Dutta, P. Horodecki, and J. Zakrzewski, At the limits of criticality-based quantum metrology: Apparent super-Heisenberg scaling revisited, Phys. Rev. X **8**, 021022 (2018).

[69] Y.-X. Wang and A. A. Clerk, Intrinsic and induced quantum quenches for enhancing qubit-based quantum noise spectroscopy, Nat. Commun. **12**, 6528 (2021).

[70] O. Bleu, G. Malpuech, Y. Gao, and D. D. Solnyshkov, Effective theory of nonadiabatic quantum evolution based on the quantum geometric tensor, Phys. Rev. Lett. **121**, 020401 (2018).

[71] T. Ozawa and N. Goldman, Extracting the quantum metric tensor through periodic driving, Phys. Rev. B **97**, 201117(R) (2018).

[72] J. Kopp, Efficient numerical diagonalization of Hermitian 3×3 matrices, Int. J. Mod. Phys. C **19**, 523 (2008).

[73] W. Ding, W. Zhang, and X. Wang, Quantum-memory-assisted precision rotation sensing, Phys. Rev. A **102**, 032612 (2020).